Leading Edge Rain Erosion and Lifetime Prediction of Advanced Polymer Coatings for Wind Turbine Blades

MSc Thesis

Chun-Yen Wu

Delft University of Technology

TU Delft

Leading Edge Rain Erosion and Lifetime Prediction of Advanced Polymer Coatings for Wind Turbine Blades

MSc Thesis

by

Chun-Yen Wu

to obtain the degree of Master of Science in Sustainable Energy Technology
at the Delft University of Technology,
to be defended publicly on July 13, 2023 at 12:30 PM.

Student number:	5537800	
Project duration:	November, 2022 – July, 2023	
Thesis committee:	Dr. ir. J. J. E. Teuwen,	TU Delft, chair, supervisor
	Dr. ir. J. A. Pascoe,	TU Delft, committee member
	Dr. D. Zappalá,	TU Delft, committee member

An electronic version of this thesis is available at http://repository.tudelft.nl/.

TU Delft

Preface

With great joy and a deep sense of accomplishment, I present this Master's thesis, the culmination of my studies in Sustainable Energy Technology at Delft University of Technology. The two-year study has been challenging but rewarding, filled with valuable experiences and knowledge.

Firstly, I want to express appreciation to my dear family. Despite the physical distance, their unwavering support and reassurance have been a constant source of strength throughout this journey. Their belief in my abilities has motivated me to overcome obstacles and strive for excellence.

I am immensely grateful to my thesis supervisor, Julie Teuwen, for her invaluable guidance, expertise, feedback, and encouragement. I enjoyed every meeting to share my ideas and receive her insightful input. Working with Julie has been an absolute pleasure, and her mentorship has played a pivotal role in shaping the quality and depth of this thesis.

Moreover, I also want to thank Amrit Verma for sharing his knowledge of the erosion model. I would like to extend my appreciation to Fernando Sánchez and Asta Šakalytė for providing information on the material used in the experiment. In addition, I want to express my gratitude to Victor Horbowiec and Pietro Marchese for their technical assistance in the laboratory.

At last, I want to thank all my friends who have accompanied me on this journey. Their presence, both on and off campus, has made this academic endeavor enjoyable and memorable. I will always cherish this sense of belonging and camaraderie.

Chun-Yen Wu
Delft, July 2023

Summary

The increasing focus on sustainable living and the need to reduce dependency on fossil fuels has led to a growing interest in renewable energy sources. Among these, the wind energy sector has not only experienced significant growth in terms of numbers but also in size. Larger turbines lead to more severe leading-edge erosion and further increase operation and maintenance costs. To mitigate this problem, the new advanced leading-edge protection has become vital in the wind energy sector. This thesis focuses on the evaluation of two polymer coating materials (PA and PD) using a Pulsating Jet Erosion Test (PJET) setup.

The first aim of this thesis is to propose a novel analysis method to address the issue of volume interdependence in the PJET. To achieve this, a concept called ”equivalent velocity” is introduced. The equivalent velocity represents the velocity at which a spherical droplet should impact a surface to exert the same kinetic energy per impingement as the actual water slug moving at the impact velocity. By utilizing this concept, the velocity-number of impacts plot takes into account the volume interdependence in erosion experiments.

The second aim is to utilize the PJET to analyze the erosion behavior of PA and PD coatings. The investigation focuses on understanding the relationship between impact velocity and the number of impacts until the incubation period and the breakthrough. The incubation period refers to the interval until the damage is visible and the breakthrough is the moment until the filler underneath the coating is exposed. Additionally, the erosion damage progression of the coatings was analyzed, and the lifetime prediction was evaluated using an existing long-term leading-edge rain erosion model.

The experimental results revealed that the ductile material (PD) exhibits a longer resistance to erosion compared to the stiff material (PA), with the mean number of impacts until breakthrough being 2 to 3 times higher for PD. Moreover, the long-term leading-edge rain erosion model highlights the importance of the accurate measurement of material properties, as lifetime prediction is very sensitive to ultimate tensile strength and Poisson’s ratio.

However, it is crucial to validate the equivalent velocity method through experiments and numerical modeling, while also improving the experimental method to allow for continuous observation of the erosion process in a controlled environment with temperature and humidity regulation. Conducting tests in a wider range of velocities is also recommended. Additionally, improvements for the rain erosion model are necessary to accommodate the utilization of the equivalent velocity.

Contents

List of Figures

List of Tables

Acronyms

DSD Droplet size distribution. 11

IEA International Energy Agency. 1

KNMI Koninklijk Nederlands Meteorologisch Instituut. 11

LEP Leading edge protection. 1, 7

O&M Operation and maintenance. 3

PDF Probability density function. 11

PJET Pulsating Jet Erosion Test. 7

WARER Whirling Arm Rain Erosion Rig. 7

Nomenclature

$\dot{D}_i^{ST}(I, d, U_W)$ Short-term erosion damage rate ($\frac{1}{hr}$)

α Angle ($^\circ$)

α Impact angle ($^\circ$)

β Angle ($^\circ$)

β Droplet impingement efficiency (-)

$\dot{D}_i^{LT}$ Long-term erosion damage rate ($\frac{1}{hr}$)

κ Shape parameter (-)

ν Poisson's ratio (-)

ω Angular velocity of the disc ($\frac{^\circ}{s}$)

$\overline{q}$ Number of droplets per unit volume of rainfall ($\frac{1}{m^3}$)

ρ_C Density of coating ($\frac{kg}{m^3}$)

ρ_L Density of water ($\frac{kg}{m^3}$)

σ_a Stress amplitude (Pa)

σ_U Ultimate tensile strength (MPa)

θ Angle between the center of the water jet and the center of the hole in terms of the center of the disc ($^\circ$)

A Cross-sectional area (m^2)

a Wind shear exponent (-)

$A_{complete}$ Complete overlap region (m^2)

$A_{incomplete}$ Incomplete overlap region (m^2)

b_1 Constant (-)

c Scale parameter ($\frac{m}{s}$)

d Droplet size or droplet diameter (mm)

f Impact frequency (Hz)

$f_I(I)$ Marginal distribution of rainfall intensity ($\frac{hr}{mm}$)

h_C Thickness of the coating (mm)

I Rainfall intensity ($\frac{mm}{hr}$)

k Constant (-)

KE Applied kinetic energy per impact (J)

l Length of the assumed cylindrical water slug (m)

m	Mass of the water slug (kg)
m	Wöhler slope (-)
N	Number of cycles (-)
n	Number of impacts (-)
n_b	Number of impacts until the breakthrough (-)
n_i	Number of impacts until the incubation period (-)
$P(I)$	Percentage of rain duration for different intensities (%)
R	Distance between the center of the disc and the center of the hole (m)
r_h	Radius of the hole on the disc (m)
r_j	Radius of the cross-section area of the water jet (m)
$r_{smaller}$	Radius of the smaller circle among the hole on the disc and the cross-sectional area of the water jet (m)
S	Strength parameter (Pa)
s	Semiperimeter of the triangle (m)
T	Time until the end of the incomplete overlap region (s)
t	Expected lifetime of the blade coating system (yr)
t	Timestamp during the hole and the water jet overlap (s)
t_0	Time until the end of the complete overlap region or the beginning of the incomplete overlap region (s)
t_b	Time until the breakthrough (min)
t_i	Incubation period (min)
t_{eff}	Time to form a water slug (s)
V	Volume of the water slug (mm^3)
v	Impact velocity ($\frac{m}{s}$)
v_{blade}	Blade tip speed ($\frac{m}{s}$)
v_{eq}	Equivalent velocity ($\frac{m}{s}$)
v_{tg}	Terminal velocity of the raindrop ($\frac{m}{s}$)
v_{wind}	Wind speed ($\frac{m}{s}$)
z	Hub height (m)
z_r	Reference wind turbine height (m)
Δt	Interval between the incubation period and the breakthrough (min)
μ_I	Mean of logarithmic I (-)
σ_I	Standard deviation of logarithmic I (-)
θ	Angle between the droplet direction and the normal to the surface ($^\circ$)
C_C	Speed of sound in the coating ($\frac{m}{s}$)

C_L Speed of sound in the water ($\frac{m}{s}$)

E Young's modulus (MPa)

$f_{I,d}(I,d)$ Joint probability density function of I and d ($\frac{hr}{mm^2}$)

$f_{U_W}(v_{wind})$ Weibull distribution of the wind speed data ($\frac{s}{m}$)

m_{ref} Mass of the reference droplet (kg)

P Impact pressure (Pa)

$U_W(z)$ Mean wind speed at the hub height ($\frac{m}{s}$)

$U_W(z_r)$ Mean wind speed at the reference height of 10 m ($\frac{m}{s}$)

1

Introduction

As the consensus of sustainable living thrives, renewable energy has become the center of attention for the energy demand [46]. The literature shows the incremental trend in the renewables' share of power generation and it is projected to rise even faster to reach net zero emission [27, 33]. In particular, according to International Energy Agency (IEA) [3], wind energy has seen the most significant growth among all sustainable energy technologies, with an increase of 17% (273 TWh) in electricity produced in 2021. In addition to the increase in the number of installations, this development can be attributed to the increased hub height and size of the wind turbines as shown in Figure 1.1. The large-scale wind turbines are designed to be installed at the sites with high wind speed, so the higher the wind energy can be harnessed [25]. However, the high-speed rotation of wind turbine blades can lead to detrimental erosion caused by factors such as sand, rain, and hail [41]. This type of erosion causes cracks and cavities and occurs most severely at the leading edge area. The loss of the material deteriorates the aerodynamic performance and thus the efficiency of wind turbines drops [29]. In the research of Han et al. [24], the lift coefficient of the airfoil of a 5 MW wind turbine blade decreased by 53% and the drag coefficient increased by 314% after the erosion at the leading edge. Consequently, the overall annual energy production of one 5 MW wind turbine drops 2% to 3.7%. Moreover, the maintenance of wind turbine blades is often costly, and downtime due to repairs can incur a shortfall in energy production.

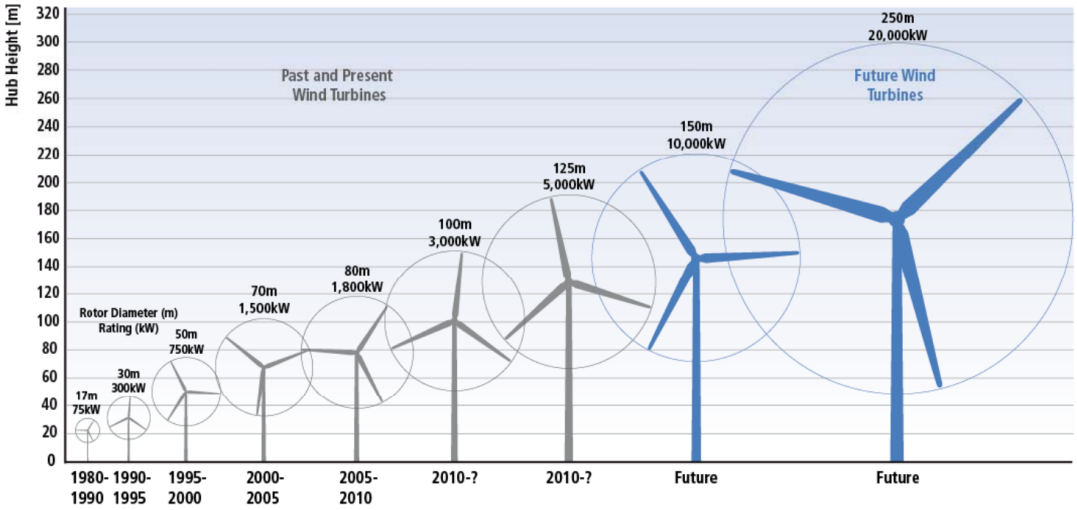

Figure 1.1: Growth in size of commercial wind turbines [18].

As a result, leading- edge protection (LEP) is important to mitigate the problem [29, 40]. Common methods include the application of coating layers, leading edge tapes, and erosion shields on the surface of wind turbine blades. These protections are typically made from viscoelastic materials, such as

polyurethane, epoxy, and polyamide, that possess a balance of stiffness and flexibility. 3M states that a designed wind protection tape can withstand 6 to 8 years [20]. Even a lifetime of 10 years is projected for some materials [17]. Yet, none of them can reach the wind turbine design of 25 to 30 years [39]. Consequently, time-consuming and labor-intensive maintenance is required where technicians need to be craned to the top of the turbine so that they can abseil down to the specific problem area [50]. Given these issues, many manufacturers continue to develop more erosion-resistant coating materials to reduce the frequency of repairs over the lifespan of wind turbines.

This report aims to conduct rain erosion tests on two different coating materials (PA and PD) and compare their performance in terms of material properties. The findings will enhance our understanding of erosion behavior and contribute to the future development of LEP coatings.

The remaining part of the report is structured into several chapters. In chapter 2, the literature review on water droplet erosion and blade surface protection is introduced. Two types of rain erosion test facilities are described and the post-processing methods of experimental results. Also, lifetime prediction models used in the study are illustrated. Chapter 3 presents the methodology for experiments and the long-term leading-edge rain erosion model and explains a proposed method to interpret test results. Chapter 4 analyzes the implementation of the proposed method tackling the volume interdependence of parameters on previous experimental results and provides results and discussion regarding experiments and modeling. Lastly, chapter 5 provides conclusions of the study by answering the research questions, and recommendations for future investigation are depicted in chapter 6.

2

Background knowledge

This chapter provides a literature review of the study of rain erosion on wind turbine blades. Section 2.1 provides the definition of leading edge rain erosion on wind turbine blades. Section 2.2 explores the various erosion mechanisms involved in the degradation of coatings. In section 2.3, the factors that influence the rate of erosion are discussed, including impact and environmental conditions. Section 2.4 delves into the coating systems used on wind turbine blades, presenting their composition and application methods. Section 2.5 presents an overview of two common types of rain erosion testing facilities employed to evaluate coating performance. The expressions of their experimental results are discussed in section 2.6. In section 2.7, a state-of-the-art long-term lifetime prediction model for rain erosion is introduced. Finally, section 2.8 defines the scope of this research, outlining the objectives and research questions to be addressed.

2.1. Leading edge rain erosion on wind turbine blades

Wind turbine blades are commonly made of fiber-reinforced plastic composite material, which offers a combination of high strength, high stiffness, and low weight, making it economically viable [31, 35, 41]. Yet, these materials are susceptible to degradation from environmental impacts such as rain, sand, and hail. As particles strike the surface of wind turbine blades, they can cause pits, cracks, and other forms of damage [53]. The damage, defined as erosion, compromises the aerodynamic performance of the turbine and leads to increased operation and maintenance (O&M) costs [49]. The leading edge of the blade is particularly vulnerable to severe erosion [51], as shown in Figure 2.1.

Figure 2.1: Leading edge erosion of wind turbine blades [19].

Raindrops are among the primary causes contributing to leading edge erosion. Thus, it is crucial to understand the impact event of raindrops in order to develop effective techniques to slow down erosion. The following section lays out the mechanisms of erosion damage. To develop effective mitigation strategies, it is essential to explore the underlying mechanisms of erosion damage.

2.2. Erosion mechanisms

This section reviews three erosion mechanisms in rain erosion. The phenomenon of water hammer pressure is explained in subsection 2.2.1, highlighting its role in generating intense pressure upon impact. In subsection 2.2.2, lateral jetting and its impact on surface material removal and crack growth are addressed. The influence of stress waves on the material surface is then discussed in subsection 2.2.3, emphasizing their ability to accelerate fracture formation. Through a comprehensive understanding of these erosion mechanisms, insights into the underlying processes of rain erosion can be gained.

2.2.1. Water hammer pressure

The phenomenon of water hammer pressure is a result of rapid internal deceleration of water droplets, which in turn produces intense pressure [7]. Taking the angle between the direction of the droplet and the normal to the surface (θ) into account, Cook's equation to determine the water hammer pressure can be derived [8]:

$$P = \rho_L C_L v cos\theta \tag{2.1}$$

The density of water, the speed of sound in the water, and the impact speed are represented by ρ_L, C_L, and v respectively.

2.2.2. Lateral jetting

After the water hammer pressure, the droplet starts to deform and change its direction laterally as shown in Figure 2.2. This lateral jetting is triggered by the pressure difference across the free surface at the contact edge region [23]. The velocity of lateral jetting increases as the impact velocity increases [42]. It can move at a velocity significantly greater than its initial impact speed [34]. A study simulating a droplet impacting on a leading edge coating system demonstrates that the velocity of the lateral jet is raised by 2 to 4 times compared to the impact velocity [58]. Due to the high velocity, the lateral jet has the capability to remove unevenness on the surface material, thereby facilitating the growth of cracks after the incubation period [43]. Although there are several investigations of the lateral jetting behavior, the understanding of its nature is still limited [31].

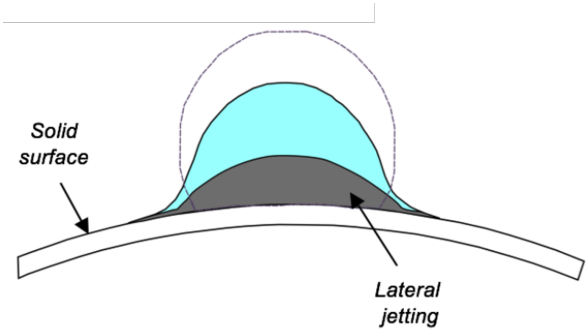

Figure 2.2: Lateral jetting on the solid surface [57].

2.2.3. Stress waves

In addition, the stress waves occur after the impact, resulting in an imbalance in the material, leading to the movement of particles to adjust to the imposed stress. A stress wave is a type of acoustic wave that travels through solid materials at a determined speed [59]. Stress waves can be categorized into three types: shear waves, compressional waves, and Rayleigh waves [31], as presented in Figure 2.3. A shear wave propagates in a transverse direction, meaning that the energy propagates into the surface via particles moving perpendicularly. A compressional wave travel in a longitudinal direction, parallel

to the direction of wave propagation. The particles of the material move in the same direction as the wave. The compressional wave has the least destructive ability among the three. Rayleigh waves travel along the surface of a material and have circular motion, causing particles to move in orbits. Rayleigh waves lead to asperities on the surface and have the largest effect on causing damage [12]. The speed, direction, and magnitude of stress waves are affected by the properties of the medium such as elasticity, density, and Poisson's ratio. The stress waves expedite the formation of fractures. To include the effect of stress wave behavior on the impacted non-rigid surface such as blade coatings, the modification of the impact pressure for erosion becomes

$$P = \frac{\rho_L C_L v cos\theta}{1 + \frac{\rho_L C_L}{\rho_C C_C}} \tag{2.2}$$

where ρ_C and C_C are the density of the coating and the speed of sound in the coating [13].

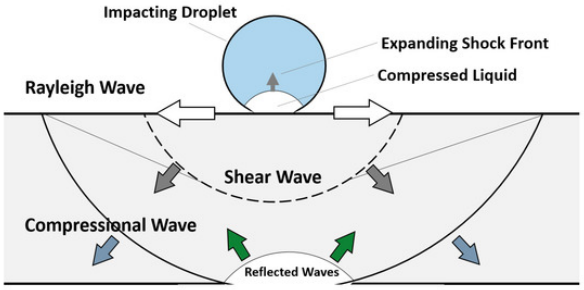

Figure 2.3: Representation of different types of stress waves: shear wave (transverse), compressional waves (longitudinal), and Rayleigh wave (surface) [31].

2.3. Factors influencing the rate of erosion

It is also important to look into parameters that influence rain erosion. This section begins by discussing the impact conditions, specifically the droplet size, impact velocity, and impact frequency. Additionally, the environmental conditions including temperature and humidity are also presented.

2.3.1. Droplet size

The diameter of raindrops is influenced by various meteorological and atmospheric conditions [31]. As a result, raindrop size distribution is typically not uniform and can be better described by a continuous probability distribution, which indicates the number of raindrops with a specific diameter per unit volume of air. Furthermore, researchers have found that the droplet size distribution is a function of droplet diameter and rainfall intensities.

The size of droplets ranges from small droplets found in clouds (with a diameter of less than 0.1 mm) to larger droplets reaching up to 6 mm in diameter [2]. Many researchers studying rain erosion have selected the use of a droplet diameter of 2 mm for erosion tests [1]. It is also motivated by the fact that it corresponds to the mean droplet diameter at a rainfall intensity of 25.4 $\frac{mm}{hr}$, which is classified as heavy rain. Fyall [21] stated that 2 mm droplet size is a balance struck between the more pronounced individual effects of larger droplets and the greater number of impacts caused by smaller droplets.

2.3.2. Impact velocity

The impact velocity (v) at the leading edge of the blade tip is determined by the peripheral speed of the tip (v_{blade}), the terminal velocity of the incoming rain drops (v_{tg}), and the wind speed (v_{wind}). Since the three types of velocity are not the same, the calculation is based on vector as shown in the following:

$$\overrightarrow{v} = \overrightarrow{v_{blade}} - \overrightarrow{v_{tg}} + \overrightarrow{v_{wind}} \tag{2.3}$$

The terminal velocity of the droplet at the ground level is determined by the size of the droplets, which is written as the empirical equation [5, 53]

$$v_{tg} = 9.65 - 10.3e^{-0.6d} \tag{2.4}$$

where d represents the diameter of the droplet. From Figure 2.4, it can be observed that the terminal velocity reaches a plateau of approximately 9.6 $\frac{m}{s}$ as the droplet grows larger.

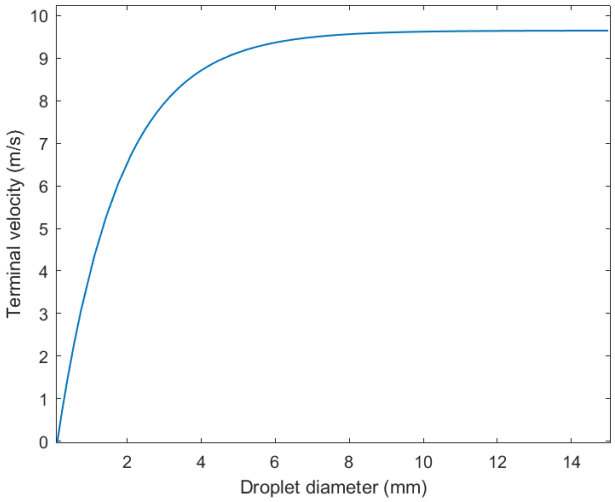

Figure 2.4: Terminal velocity of free-falling droplet as a function of droplet diameter.

However, the terminal velocity of a free-falling rain droplet has little effect on wind turbine blade leading-edge erosion compared to the blade tip speeds [41].

2.3.3. Impact frequency

The higher the impact frequency (f) is, the shorter the time for the damage to occur, as it is faster to reach the number of impacts until the failure of materials. Besides, the impact frequency plays an important role in erosion for viscoelastic materials. It influences the extent of material can recover from deformation prior to the next impingement. If the droplets impact the coating at a high frequency, such that the time between impacts is shorter than the material's ability to return to its original state, it results in a buildup of strain in the coating and causes it to fail [62].

2.3.4. Impact angle

The impact angle of water droplet erosion refers to the angle at which the droplets strike a surface, as shown in Figure 2.5. Research shows that this angle can affect the mass loss rate of materials under erosion [10, 26]. In the investigation of A. S. Verma et al. [58], the impact of rain droplets at angles between 50° and 90° is particularly critical under heavy rainfall conditions, and the resulting impulse peaks at 90°. As the angle decreases, the impulse decreases accordingly.

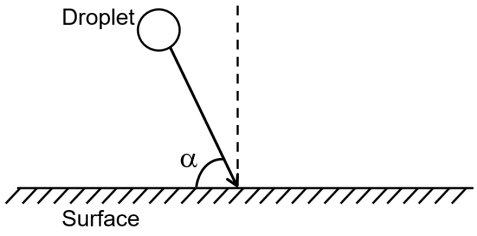

Figure 2.5: Impact angle of a water droplet where α is the impact angle and the dashed line is the surface normal.

2.3.5. Temperature

Temperature affects the properties of the droplets and the materials being impacted. Rising temperature results in a higher erosion rate [52, 61]. The previous research done by M. Alonso Diaz [14]

demonstrates that the number of impacts until failure decreases as the temperature increases gradually toward stability for the polyurethane coating.

2.3.6. Humidity

Literature points out that the composite materials are susceptible to moisture [41, 61]. Different humidity in the surroundings leads to different water uptake of the material. The experiment indicates that the higher the water uptake the faster the damage occurs for polyurethane [14].

2.4. Coating system for wind turbine blades

To make wind turbine blades endure longer from leading edge rain erosion, leading edge protection (LEP) is a pivotal solution. LEP usually refers to the application of tapes or coatings onto the leading edge. There are two common techniques to apply coatings on blades [41]. The first method is called in-mold application where the gelcoat is applied on the surface of the mold prior to infusing the resin for the composite material for the blade. The gelcoat, made of similar materials as the base resin in the blade, such as epoxy and polyester, forms a strong chemical bond with the blade. The other technique is the post-mold application, which involves applying the coating onto the blade's surface after the molding process. This allows a wider selection of coating materials. However, the post-mold application is a highly time-consuming process due to the need for surface finishing. In the case of LEP against rain erosion, the post-mold application is typically employed [9]. The post-mold application is a multilayered system as shown in Figure 2.6. Before applying the coating material, the filler is first applied on the substrate laminate so as to prepare a smooth surface [45]. The filler helps fill defects and remove undulations. Sometimes a primer layer is added between the filler and coating to enhance the adhesion.

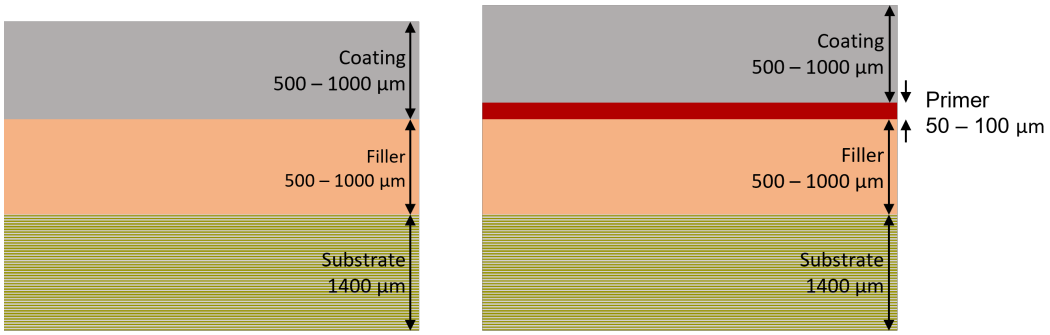

Figure 2.6: Two examples of the multilayer configuration of wind turbine blades. Left consists of substrate laminate, filler, and coating, while there is an additional primer layer in the right [16].

2.5. Rain erosion testing

In order to evaluate the performance of the coating for LEP, inter-laboratory testing is essential. There are two test facilities are commonly employed: the Whirling Arm Rain Erosion Rig (WARER) and the Pulsating Jet Erosion Test (PJET) setup [54]. Both are designed to accelerate the erosion of the test material. In Figure 2.7, the WARER works by using a spinning arm that has a test sample mounted at the tip. The arm is accelerated up to the designed speed. To simulate rainfall, 36 needles on top release droplets onto the sample.

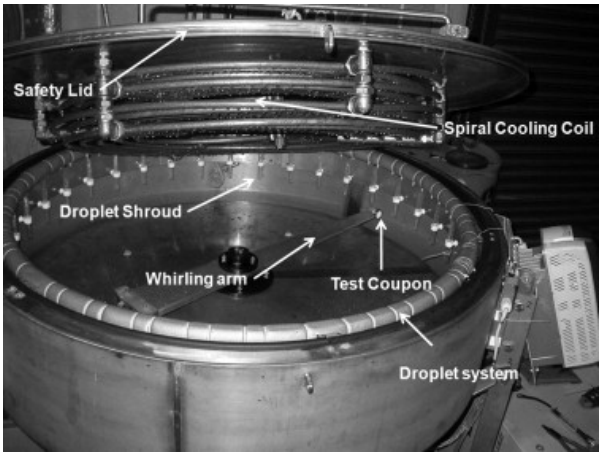

Figure 2.7: WARER [54].

Figure 2.8 demonstrates the working principle of the PJET. A continuous water jet through a nozzle is produced by a high-pressure pump. The water jet then encounters a rotating disc with two holes. When the holes intermittently align with the path of the jet, the water jet is cut into water slugs hitting the sample.

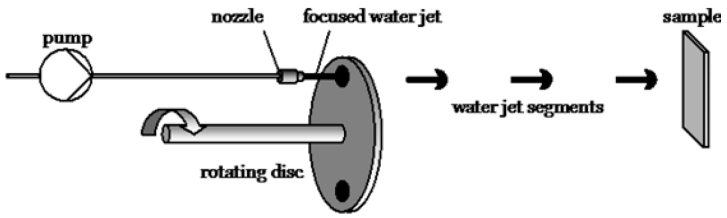

Figure 2.8: Working principle of the PJET [54].

For WARER, characterizing the damage in terms of the number of impacts at a specific location of the sample is challenging since the continuous droplets that come out of the needles are likely to fall all over onto the upper camber and the leading edge of the airfoil. However, for PJET, the sample is fixed and the impact spot is at the same position, allowing for precise determination of the number of impacts at that point. The advantage of WARER is that it can provide fixed droplet size and volume, unaffected by other parameters such as impact velocity and rainfall intensity. In contrast, PJET is subject to variations in water slug size due to different impact velocities and impact frequencies. When the impact velocity is higher, the amount of water passing through the hole per unit time increases. When the frequency is higher (indicating faster rotation of the disc), the time for each water slug to pass through the hole decreases, resulting in smaller cut-out water slugs. This leads to a dependence of water slug volume on impact velocity and impact frequency. It is crucial to acknowledge that the volume of each water droplet varies as the impact velocity and impact frequency are adjusted. However, the current representation of these parameters in relation to the number of impacts overlooks this aspect.

2.6. Results of rain erosion testing

Experimental evidence illustrates that water droplet erosion is a time-dependent phenomenon [31]. Using the rain erosion test facilities, the mass loss of the coating system over the number of impacts or time can be measured and plotted as Figure 2.9. It can be categorized into three phases [53]. In the beginning, there is an interval where the damage can hardly be measured, known as the incubation period. The incubation period refers to the exposure time until the first damage is visually detectable. Following the incubation period, the weight loss of the material increases roughly linearly with time, indicating the phase of a steady rate erosion region. In this stage, the erosion rate is relatively constant,

and the protective covering is gradually being eroded by the water droplet impacts. After a certain period of time, the breakthrough is reached. The breakthrough is defined as the moment when the coating is penetrated and the underlying filler is exposed. The phase afterward is called the final erosion region.

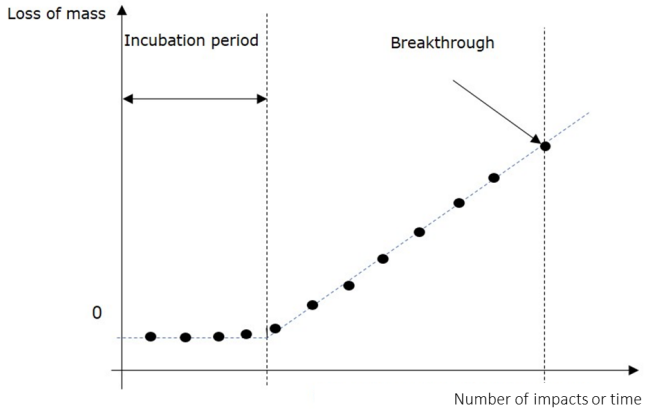

Figure 2.9: Erosion graph indicating different erosion stages. Adjusted from [15].

An example of the progression of damage in LEP samples, comprising a coating, filler, and substrate, observed via X-ray computed tomography is displayed in Figure 2.10. Prior to erosion (Figure 2.10a), the sample surface appears flat and undamaged. Then, Figure 2.10b shows the damage until the incubation period where the initial damage on the coating is observed. Finally, in Figure 2.10c, significant portions of the coating are removed, revealing the filler directly from the top surface, marking the moment of breakthrough.

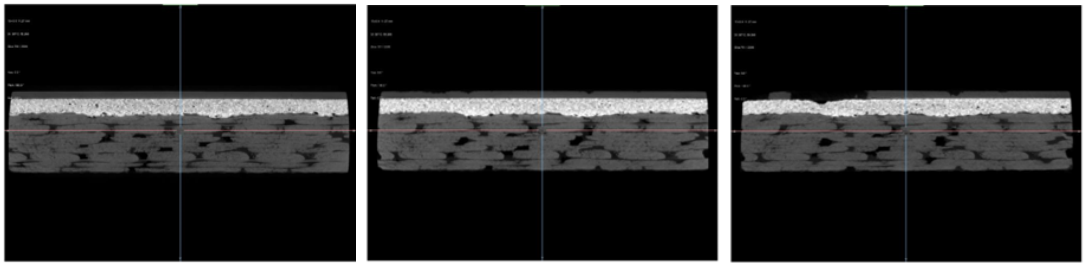

(a) Before erosion **(b)** Erosion until the incubation period **(c)** Erosion until the breakthrough

Figure 2.10: Images of samples from different erosion stages [44].

Another method to analyze the experiment is to plot the $v - n$ curve, which represents the relationship between the impact velocity (v) and the number of impacts until the incubation period (n_i) or the breakthrough (n_b). In Figure 2.11, the plot follows a power law relationship as described in the DNVGL standard [15], which is expressed as

$$n = kv^{-m} \tag{2.5}$$

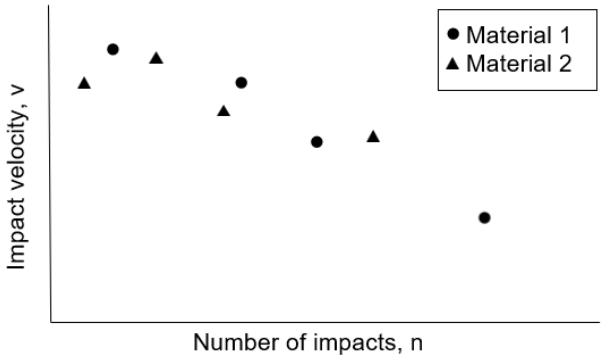

Figure 2.11: Schematic of the $v - n$ curve for the obtained data (with the logarithmic scale on the n-axis). Adjusted from [15].

where k and m are the parameters that fit the curve. This $v - n$ curve mirrors the classic Wöhler curve (Equation 2.6) used in fatigue analysis.

$$N = b_1 \sigma_a^{-m} \tag{2.6}$$

where b_1 is constant, σ_a is stress amplitude, and m is the slope of the Wöhler curve.

2.7. Lifetime prediction model

Based on the experimental results, semi-empirical erosion models have been developed for the lifetime prediction of coated materials. One widely used model - Springer's model - describing surface fatigue is shown subsection 2.7.1. Based on Springer's model, a long-term leading edge erosion model is introduced in subsection 2.7.2.

2.7.1. Springer's model

To understand surface erosion, G. S. Springer [53] gathered available experimental data from various rain erosion facilities including PJET to create a model to project the incubation period. The concept is from the traditional Wöhler curve since a repetitive process of stress cycles caused by the impact of liquid droplets resembles fatigue accumulates in mechanical components subjected to cyclic loading. The model demonstrates the number of impacts per site until the incubation period (n_i) in association with the properties of the material and the impact conditions. This relationship is presented in Equation 2.7, where S is the strength parameter and P is the impact pressure from Equation 2.2.

$$n_i = 7 \times 10^{-6} (\frac{S}{P})^{5.7} \tag{2.7}$$

The strength parameter has the following expression

$$S = \frac{4\sigma_u(m-1)}{1-2\nu} \tag{2.8}$$

consisting of the material properties: ultimate tensile strength (σ_u), Poisson's ratio (ν), as well as the slope of the Wöhler curve (m) which can be obtained from rain erosion experiments. Note that the expressions presented here are specifically applicable to the erosion of homogeneous materials. Springer's model for coated materials follows the same framework but incorporates modifications to consider stress wave reflections into the coating at the coat-substrate interface [53].

There are some limitations that apply to Springer's model:

- With the same logic as the traditional Wöhler curve, the model assumes that the number of impacts must be greater than one, as failure under a single impingement is not representative. This is called the lower limit, expressed by the condition:

$$n_i > 1 \quad \text{or} \quad \frac{S}{P} > 8 \tag{2.9}$$

- For all the considered experimental data used in the model, the measured number of impacts until the incubation period (n_i) does not exceed three times Springer's analytical equation. This is defined as the upper limit, as given by:

$$n_i < 21 \times 10^{-6} (\frac{S}{P})^{5.7} \tag{2.10}$$

- Stress wave reflections are neglected in the coating. Therefore, the thickness of the coating (h_C) should be sufficiently large, as determined by:

$$h_C > 2d\frac{C_C}{C_L} \tag{2.11}$$

  where d is the droplet diameter, C_C is the speed of sound in the coating, and C_L is the speed of sound in the water.

Additionally, a sensitivity study of Springer's model was carried out by N. Hoksbergen et al. [30]. The number of impacts until the incubation period in Springer's model was found to be most sensitive to Poisson's ratio, coating material strength, and empirically fitted constants. For instance, a higher Poisson's ratio with the other parameters fixed results in longer lifetime predictions. However, the physical interpretations and meanings behind these relationships are still not fully explored. These findings highlight the need for caution when using Springer's model.

2.7.2. Leading edge erosion model

The experimental $v - n$ curve and Springer's surface fatigue model can predict the lifetime of a coating material by providing the number of impacts it can endure at a given velocity. However, it is important to note that the actual longevity of the coating on a wind turbine in operation is influenced by rainfall intensity, droplet size, probability of precipitation, wind speed, rotational speed of the turbine, etc. To address this challenge, a site-specific long-term erosion model developed by A. S. Verma [56] is useful to project the coating lifetime in real-world scenarios, expressed in years. The model is a site-specific model which consists of rain and wind data from 31 locations acquired from Koninklijk Nederlands Meteorologisch Instituut (KNMI). After a series of modeling demonstrated in Figure 2.12, the lifetime of the coating is predicted. The components of this model are described as follows:

- Probabilistic rain model:
  It is described by the joint probability density function (PDF) of rain droplet size (d) and rainfall intensity (I) since d and I are dependent variables. This joint PDF is defined by the following equation:

$$f_{I,d}(I, d) = f_I(I) \cdot f_{d|I}(d|I) \tag{2.12}$$

  where $f_I(I)$ is the marginal distribution of rainfall intensity and $f_{d|I}(d|I)$ is the droplet size distribution (DSD). $f_I(I)$ is described by the lognormal distribution based on the site:

$$f_I(I) = \frac{1}{\sqrt{2\pi}\sigma_I} e^{\frac{-(ln(I)-\mu_I)^2}{2\sigma_I^2}} \tag{2.13}$$

  However, the DSD is not site-specific due to the lack of disdrometer measurements. Consequently, Best's DSD [6] is employed in this model:

$$F_{d|I}(d|I) = 1 - e^{-(\frac{d}{1.3I^{0.232}})^{2.25}} \tag{2.14}$$

- Wind statistics model:
  It involves choosing the most suitable distribution to fit the mean wind speed at the hub height of wind turbines. Since the available data is recorded at a reference height of 10 m, the mean wind speed at the target hub height can be approximated using the power law:

$$U_W(z) = U_W(z_r) \cdot (\frac{z}{z_r})^a \tag{2.15}$$

where z is the hub height, z_r is the wind speed at the reference height of 10 m, and a is the wind shear exponent. Weibull distribution is used to represent wind statistics, which is given by

$$f_{U_W}(v_{wind}) = \frac{\kappa}{c}(\frac{v_{wind}}{c})^{\kappa-1}e^{-(\frac{v_{wind}}{c})^{\kappa}} \tag{2.16}$$

- Wind turbine model:
  It is built upon the type of wind turbines selected. This includes the relationship between rotor speed and the mean wind speed. The rotor speed directly determines the speed of the blade which is the main factor of the impact velocity. Furthermore, descriptions of the turbine, such as the length of the blades and the hub height, are necessary for the calculation.

- Material model:
  As the long-term erosion model utilizes Springer's equation (Equation 2.7) which will be later explained in the analytical surface fatigue model, the coating properties serve as inputs since S (Equation 2.8) and P (Equation 2.2) are involved. These properties are density (ρ_C), speed of sound (C_C), ultimate tensile strength (σ_U), and Poisson's ratio (ν) which are obtained from specifications or experimental measurements. The remaining Wöhler slope (m) is acquired from the experimental results of rain erosion tests as introduced in section 2.6.

- Analytical surface fatigue model:
  The analytical model first considers the short-term erosion damage rate ($\dot{D}_i^{ST}(I, d, U_W)$ in hr^{-1}), which is based on Springer's model. Thus, this rate demonstrates continual accelerated erosion without considering meteorology (rain and wind). The short-term erosion damage rate is defined by

$$\dot{D}_i^{ST}(I, d, U_W) = \frac{\overline{q}v\beta}{\frac{8.9}{d^2}(\frac{S}{P})^{5.7}} \tag{2.17}$$

  where v represents the impact velocity (neglecting the wind speed term in Equation 2.3). $\overline{q}$ is the number of droplets per unit volume of rainfall, expressed as

$$\overline{q} = 530.5\frac{I}{v_{tg}d^3} \tag{2.18}$$

  where I is the rainfall intensity. β is droplet impingement efficiency presenting the fraction of droplets that will hit the blade during rotation which is given by

$$\beta = 1 - e^{-15d} \tag{2.19}$$

  The denominator in Equation 2.17 is derived from Equation 2.7 divided by the impact area of a droplet ($\frac{\pi d^2}{4}$).

  At last, the long-term erosion damage rate ($\dot{D}_i^{LT}$) is computed as the weighted sum of the short-term erosion damage rate including rain and wind conditions in the following:

$$\dot{D}_i^{LT} = \sum_i^{\infty}\sum_j^{\infty}\sum_k^{\infty}\dot{D}_i^{ST}(I, d, U_W)\cdot f_{I,d}(I_i, d_j)\cdot P(I_i)\cdot f_{U_W}(U_{W_k})\Delta I\Delta d\Delta U_W \tag{2.20}$$

  $P(I_i)$ is the percentage of rain duration for different intensities. When $\dot{D}_i^{LT} \geq 1$, the incubation period of the coating is reached. Finally, the predicted lifetime (t) is defined by

$$t = \frac{1}{\dot{D}_i^{LT}\cdot(365\cdot 24)} \tag{2.21}$$

  Here, $\dot{D}_i^{LT}$ is in hr^{-1} and t is in years. Hence, the lifetime of the coating on wind turbine blades is regarded as the incubation period in a real-life operational scenario.

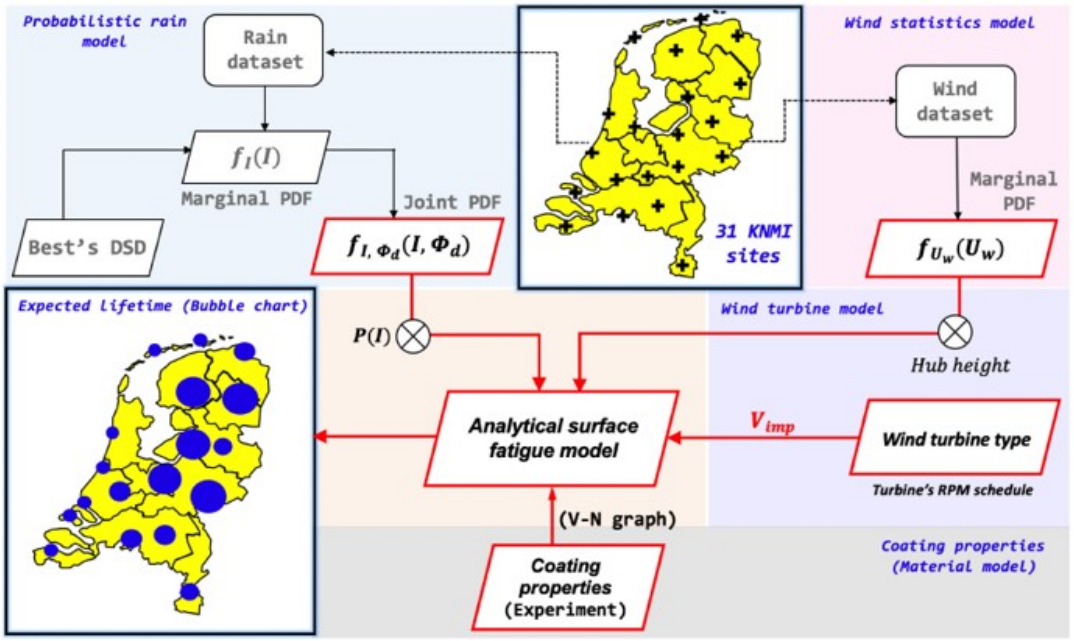

Figure 2.12: Schematic of the leading edge erosion model [56].

2.8. Research definition

It is important to understand what types of material properties are influential in improving the performance of LEP for future development. Therefore, the behavior of newly developed coating materials needs to be characterized by an experimental approach, together with the lifetime prediction by the long-term rain erosion model. In addition, it is essential to examine whether the erosion model is valid for new types of materials.

To conduct the performance analysis of coating materials against rain erosion, the PJET facility is employed in this research. However, due to the working principle of the PJET (in chapter 3), the size of the water droplet depends on the nozzle size, the speed, and the frequency. This inconsistency in droplet size can cause biased results of the number of impacts until failure if the variable parameter is set to the impact velocity or the impact frequency. To address this issue, the first objective of this master's thesis is

"to propose a new analysis approach using the applied kinetic energy concept to correct for the volume interdependence with the impact velocity and the impact frequency in the PJET"

To understand the performance of different material properties of coatings, two advanced polymer coating materials, PA and PD, are investigated in a laboratory environment and by Verma's long-term rain erosion model [55, 56]. Thus, the second objective is

"to investigate the influence of varying impact velocities on the damage behavior of PA and PD using the PJET and to predict their lifetime via the leading-edge erosion model."

In an effort to accomplish the research objectives, the following questions will be addressed:

Research question 1: How does the relationship between impact velocity and the number of impacts until failure affect the interpretation of surface fatigue in PJET results, and what alternative method can better describe this surface fatigue?

Research question 2: How do the PA and PD samples perform under the PJET in terms of the incubation period and the breakthrough?

Research question 3: How do PA and PD samples behave throughout the erosion progression until the breakthrough?

Research question 4: How can the long-term lifetime of PA and PD be predicted, and what are their long-term lifetimes?

Research question 5: How sensitive is the lifetime of PA and PD to variations in ultimate tensile strength and Poisson's ratio in the long-term rain erosion model?

3

Methodology

In this chapter, the methodology employed in the investigation of leading edge rain erosion and lifetime prediction of PA and PD coated samples is presented. Section 3.1 provides a description of the two coatings and the facilities used to test and observe samples. The test plan for operating the PJET is outlined in section 3.2. The calculation of the equivalent velocity is explained in section 3.3. Lastly, Section 3.4 presents the modeling approach used to project the lifetime of the coatings for wind turbine blades.

3.1. Test setup

This section provides an overview of the experimental setup. First, the samples used in the experiment are described, along with their properties and the test matrix on each sample. Then, the PJET is introduced, highlighting the parameters chosen for the experiment and the working principle. Finally, the Keyence VR-5000 microscope is presented as the tool used to observe and analyze the damage characteristics on the samples.

3.1.1. Test samples

The two types of coatings, PA and PD, applied on the same filler-substrate layer were used in the experiment. An example of a sample is shown in Figure 3.1a. A random selection of PA and PD samples from each batch was measured. The size of the samples was determined using a caliper and found to be 83±5 mm by 81±5 mm. The thickness of each layer was measured using a 3D microscope (as described in subsection 3.1.3). The sample was placed on the platform, which was set as the reference height (0 mm). The point height of each layer was then measured, as illustrated in Figure 3.1b. By subtracting the point heights, the thickness of each layer was obtained. The coating, filler, and substrate were found to have thicknesses of 0.25±0.09 mm, 0.86±0.05 mm, and 1.22±0.05 mm, respectively.

The test matrix of the sample is shown in Figure 3.1c. Each sample provides 16 spots (4 by 4) for each measurement. Every spot is situated at a distance away from one another and the edge in order to eliminate the edge effect and leave sufficient margin for clamping the sample.

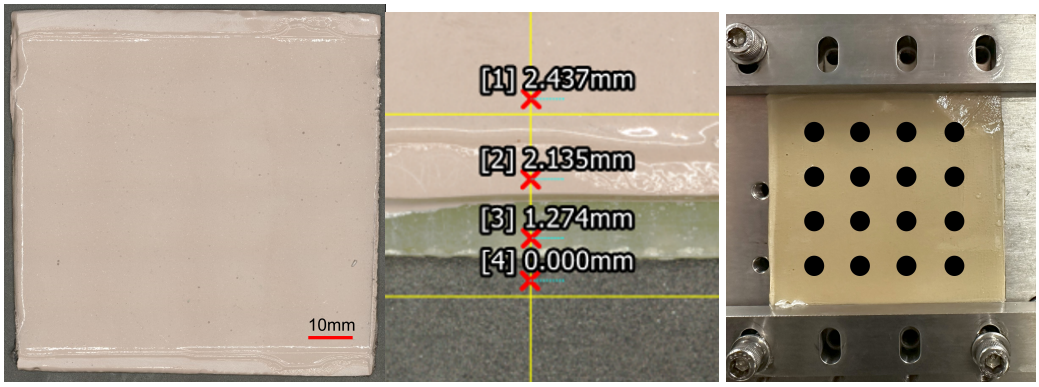

(a) (b) (c)

Figure 3.1: (a) PD sample and (b) its point height of [1] coating, [2] filler, and [3] substrate at a [4] flat surface. (c) Test spots in each sample.

The important properties of the coatings, including density (ρ_C), speed of sound (C_C), Young's modulus (E), ultimate tensile strength (σ_U), and Poisson's ratio (ν), are presented in Table 3.1. With the bulk materials of PA and PD, their densities were obtained from Archimedes' principle, while the others are based on literature [22, 28].

Table 3.1: Properties of the materials [22, 28].

	$\rho_C(\frac{kg}{m^3})$	$C_C(\frac{m}{s})$	$E(MPa)$	$\sigma_U(MPa)$	ν
PA	1133	1807	7	2.69	0.3
PD	1071	1710	1	2.11	0.3

3.1.2. Pulsating Jet Erosion Test (PJET)

To test the performance of the samples under rain erosion, the PJET provided by DUCOM is employed, as shown in Figure 3.2. However, distilled water is used rather than the actual rainwater due to the protection against corrosive substances. Table 3.2 shows the designed testing parameters of the facility.

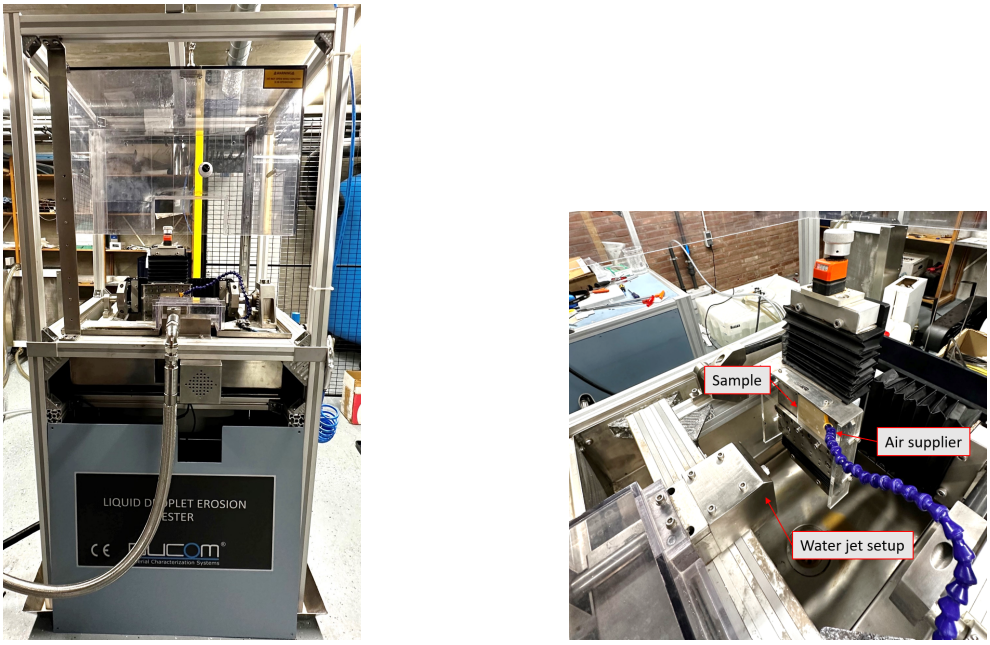

(a) (b)

Figure 3.2: (a) Ducom Liquid Droplet Erosion Tester with (b) the zoom-in view of components.

Table 3.2: Selected testing parameters for the PJET.

Nozzle size	Impact velocity	Impact frequency	Air supply	Impact angle
1.5 mm	140 - 170 m/s	42 Hz	3 bar	90 degree

The droplet size is determined by the nozzle size and the hole on the disc. For this experiment, a conventional droplet size of 2 mm is chosen. Therefore, the 1.5 mm nozzle is used which is estimated to create droplets with 2 mm diameter due to the expansion resulting from the high pressure. Meanwhile, the diameter of holes on the disc is 2 mm which can constrain the droplet size from expanding beyond 2 mm. The high-pressure pump generates impact velocities ranging from 25 to 250 $\frac{m}{s}$ with an accuracy of ±2 $\frac{m}{s}$. Impact velocities between 140 and 170 $\frac{m}{s}$ are chosen in this study to strike a balance between testing duration and immediate coating destruction. The impact frequency is controllable from 5 to 100 Hz. The air supplier provides 0 to 6 bar pressurized air stream to remove water film avoiding the water cushioning effect. In this experiment, the impact frequency and the pressure of the air supply are set at 42 Hz and 3 bars aligning with the literature [14, 38]. The sample is clamped on the sample holder 50 mm away from the nozzle to match the calibration of the velocity. The angle of the sample holder is adjustable between 15 and 90 degrees, but for this experiment, it is fixed at 90 degrees to simulate the most detrimental impact.

3.1.3. Microscope

The Keyence VR-5000 Wide Area 3D measuring system is used to observe and analyze the characteristics of the damage on the samples (Figure 3.3). Depending on the size of the damage, the microscope is set at a magnification of 12 times or 25 times to observe the surface morphology. The microscope scans through the surface from different angles capturing 3D optical images of the surface damage. Its image processing algorithms detect the erosion area and compute the loss of volume below the surface height, providing the data for the analysis of the erosion progression. Furthermore, the system produces height maps that offer a quantitative measurement of the sample's topography. The color palette used for the height maps is fixed, with $0.2\ mm$ as the upper limit, $-0.2\ mm$ as the lower limit, and $0\ mm$ as the surface height of samples.

Figure 3.3: Keyence VR-5000 Wide Area 3D measuring system.

3.2. Test plan

As the cabinet can hardly be seen through by observers due to the misty environment, the testing operation is designed by a repetitive working cycle as shown in Figure 3.4. The PJET runs creating

continuous water droplets hitting the sample for a period of time called operating time. The following interval is downtime during which the machine does not operate. The downtime allows the extent of the damage on the sample surface to be observed. The cycle continues until the incubation period or the breakthrough is reached.

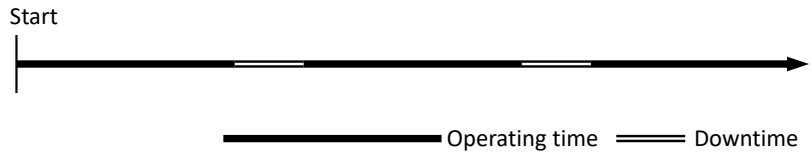

Figure 3.4: Schematic of the testing operation. X-axis represents the accumulative time from the start of activating the PJET.

The incubation period and the breakthrough are the two representative moments in erosion since they stand for the first visible fracture on the coating and the first visible penetration of the coating. Therefore, the failure of these two moments is chosen to be tested. The intervals of the operating time and downtime for the incubation test and breakthrough test are presented in Table 3.3.

Table 3.3: Operating time and downtime.

	Incubation	Breakthrough
Operating time (min)	15	60
Downtime (min)	1	1

The erosion until the incubation period of both PA and PD is performed for three impact velocities: 140, 150, and 160 $\frac{m}{s}$. Yet, the selected velocities are slightly different in the breakthrough case. We know that the breakthrough is longer than the incubation period. In addition, the experimental results of PA and PD conducted by other organizations show that PD withstands longer against erosion than PA [28]. To fit the time constraint of this study, the lowest impact velocity tested for PA is altered to 145 $\frac{m}{s}$. A higher range from 150 $\frac{m}{s}$ to 170 $\frac{m}{s}$ is set for PD. Table 3.4 displays the number of successful measurements under each condition. The outliers are excluded. The outliers are defined to be not fully damaged in terms of the incubation period and the breakthrough after testing for more than 10 hours and those damage could be observed during operation within 10 minutes.

Table 3.4: Number of successful measurements until the incubation period and the breakthrough for both coating materials at each velocity.

$v(\frac{m}{s})$	Incubation		Breakthrough	
	PA	PD	PA	PD
140	2	3	-	-
145	-	-	4	-
150	4	5	3	5
160	3	3	5	6
170	-	-	-	4

After the incubation period and the breakthrough are tested, the damage progression in between them can be investigated. This study helps us understand the rate of erosion, better identify the specific erosion mechanisms at play, and examine the changes in the LEP coating over time as a result of erosion. The experiment is conducted for two time points, $t_i + \frac{\Delta t}{3}$ and $t_i + \frac{2\Delta t}{3}$, at the velocity of 160 $\frac{m}{s}$. Here Δt is the extra time from the incubation period (t_i) till the time of the breakthrough (t_b) , that is

$$\Delta t = t_b - t_i \tag{3.1}$$

If $t_b >> t_i$, the two time points can be simplified as $\frac{\Delta t}{3}$ and $\frac{2\Delta t}{3}$. Afterward, the surface damage is evaluated using the microscope described in subsection 3.1.3. The measured volume is then multiplied by the density of the coating displayed in Table 3.1 to determine the loss of mass after erosion.

Finally, illustrating the relationship between mass loss and erosion time, can be plotted as depicted in Figure 3.5.

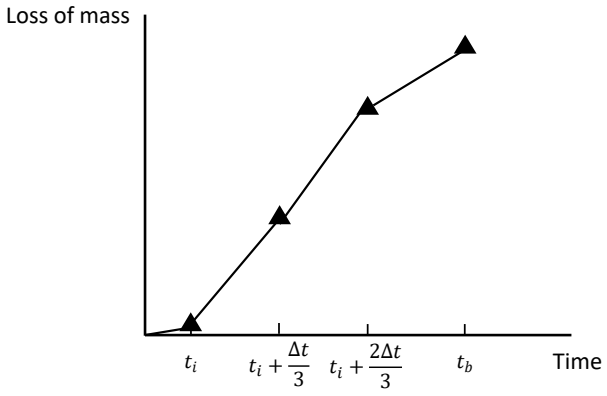

Figure 3.5: Schematic of the erosion graph developed from the experiment.

Additionally, two types of null hypotheses:

1. measurements of PA and measurements of PD under the same impact velocity have the same average number of impacts.
2. measurements under two different velocities of the same coating (PA or PD) have the same average number of impacts

are formulated to test if there is a significant difference between the average number of impacts in the two groups of measurements. The p values are used to determine whether the null hypothesis is rejected. If the p value is lower than the significance level of 0.05, the null hypothesis is rejected, indicating a significant difference between the two groups of measurements.

3.3. Equivalent velocity for PJET

The $v - n$ curve analysis of the test results obtained from the PJET lacks comprehensiveness due to the omission of the volume dependency of impact velocity, impact frequency, and disc geometry. This issue is exemplified in a previous research study [14] where three impact frequencies of 2.5, 27.7, and 42.6 Hz were investigated. It is found that the number of impacts required to cause damage is the lowest at 2.5 Hz. Yet, a higher number of impacts should be expected as the relaxation time for the viscoelastic material to recover is longer under low impact frequency. This contradiction highlights the overlooked role of volume (kinetic energy) in erosion, as stated in section 2.5 in the previous chapter.

Figure 3.6 provides a comparison between a spherical droplet and a water slug produced by the PJET from the top view. In Figure 3.6a, a reference droplet is presented as an ideal spherical water droplet with a droplet size d. Figure 3.6b demonstrates the formation of a water slug with the same droplet size when a water jet travels from the left to the right, encountering the hole of the rotating disc moving downwards. Initially, the hole intersects the water jet at the top right corner. Next, the water jet and the hole completely overlap, represented by the water slug reaching its maximum diameter (a full circle of the cross-sectional area) at the center. Subsequently, the water slug gradually tapers from the top to the bottom left, acquiring its characteristic shape.

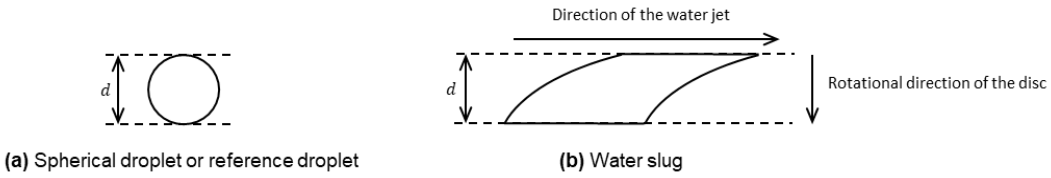

Figure 3.6: Schematic of a spherical droplet and a water slug from the top view.

In general, the volume of a water slug produced by a high-speed water jet in the PJET is larger than that of a spherical water droplet with the same diameter, as sketched in Figure 3.6. Consequently, the water slug also possesses greater kinetic energy than this moving spherical droplet at the same speed. To compensate for the disregarded variation in volume (kinetic energy) in the $v-n$ curve, while maintaining a conventional representation of impact velocity with respect to the number of impacts, the author proposed the adjusted "equivalent velocity (v_{eq})" based on the consistent reference droplet for the analysis. The concept is to consider, with the reference droplet, how high the equivalent velocity should be in order to exert the same kinetic energy per impingement as the actual one in the experiment. Hence, the following equation can be written:

$$KE = \frac{1}{2}mv^2 = \frac{1}{2}m_{ref}v_{eq}^2 \tag{3.2}$$

where KE is the applied kinetic energy per impact, m is the mass of a single water slug, and m_{ref} is the mass of the reference droplet. In this thesis, the droplet size (d) of this reference droplet is chosen to be 2 mm which is the diameter of the droplet used in the rain erosion tester as mentioned in subsection 3.1.2. Knowing the water density ρ_L, the mass of the reference droplet can be expressed as

$$m_{ref} = \frac{1}{6}\rho_L \pi d^3 \tag{3.3}$$

Before acquiring the applied kinetic energy, the volume of a water slug is considered first. The volume can be described by assuming the water slug is cylindrical as shown in Figure 3.7 [14]. First, the length (l) of this cylindrical water slug is determined by multiplying t_{eff} with the impact velocity (v) where t_{eff} refers to the interval when the water jet passes through the hole and forms a water slug. Then the volume of the water slug is the cross-sectional area of the cylinder times the length.

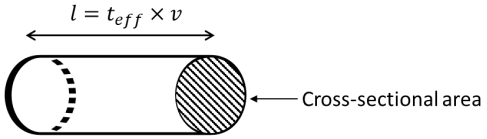

Figure 3.7: Cylindrical water slug

However, this calculation overestimates the volume since the cross-sectional area of an actual water slug varies over time. Hence, a more accurate calculation, which is named the "theoretical volume calculation", is introduced next. Firstly, the expression for overlap region (in Figure 3.8a) should be constructed. The overlap region can be categorized into two regions: complete overlap region ($A_{complete}$) and incomplete overlap region ($A_{incomplete}$). As the geometry to calculate the volume is symmetric, only half of the geometry will be used to set up the calculations.

For ease of calculation, time (t) is introduced to distinguish two overlap regions in Figure 3.8b. We set the initial position at the point where the center of the hole overlaps with the center of the water slug, which is referred to as $t = 0$. The complete overlap region starts from $t = 0$ and ends at $t = t_0$ when the region is about to shrink i.e. two circles are internally tangent, while the interval from time t_0 to T is the incomplete overlap region where T denotes the time at which the two circles no longer overlap each other i.e. they are externally tangent.

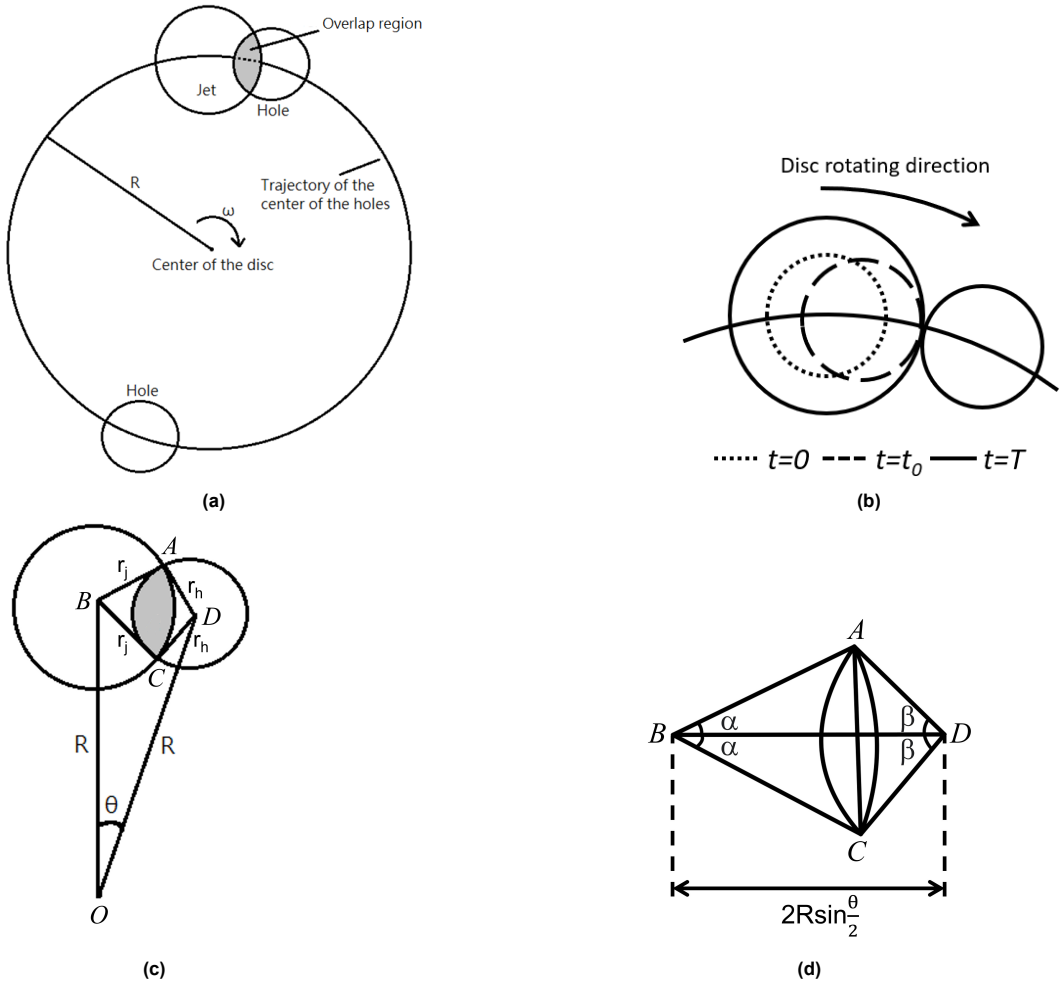

Figure 3.8: 2D geometry diagram of the disc and the water jet.

Firstly, we define the expression for these two regions. The complete overlap region ($A_{complete}$) is simply determined by the circle with the smaller radius ($r_{smaller}$) as shown in Equation 3.4. Figure 3.8c and Figure 3.8d show the incomplete overlap region ($A_{incomplete}$). It is described by the sum of the area of the circular sector ABC and ADC subtracted by the area of the kite $ABCD$ in Equation 3.5.

$$A_{complete} = \pi r_{smaller}^2 \tag{3.4}$$

$$A_{incomplete} = \frac{2\alpha}{360^\circ}\pi r_j^2 + \frac{2\beta}{360^\circ}\pi r_h^2 - 2\sqrt{s(s-r_j)(s-r_h)(s-2Rsin\frac{\theta}{2})} \tag{3.5}$$

where $\overline{AB} = \overline{BC} = r_j$ and $\overline{AD} = \overline{CD} = r_h$ represent the radius of the cross-section area of the jet and the radius of the hole. The distance between the two centers $\overline{BD}$ is $2Rsin\frac{\theta}{2}$ where R is the distance between the center of the disc and the center of the hole and θ is the angle between the center of the jet circle B and the center of the hole circle D on the trajectory. According to the law of cosines and sines, angle α and β are derived as

$$\alpha = cos^{-1}(\frac{r_j^2 + (2Rsin\frac{\theta}{2})^2 - r_h^2}{4r_j Rsin\frac{\theta}{2}}) \tag{3.6}$$

$$\beta = sin^{-1}(\frac{r_j sin\alpha}{r_h}) \tag{3.7}$$

The third term in Equation 3.5 consists of two identical triangles ($\triangle ABD$ and $\triangle CBD$) that make up a kite shape where s is defined in Equation 3.8 in reference to Heron's formula.

$$s = \frac{r_j + r_h + 2Rsin\frac{\theta}{2}}{2} \tag{3.8}$$

Since θ changes with time t as the disc is rotating, it can be expressed as

$$\theta = \omega t \tag{3.9}$$

where ω is the angular velocity of the rotating disc which is directly associated with the impact frequency (f). Since two impacts occur per rotation, the expression is

$$\omega = \frac{f}{2} \tag{3.10}$$

The volume of fluid (V) is the integration of the flow rate over the time as shown in Equation 3.11. The flow rate is the cross-sectional area (A) times the flow velocity. Lastly, the value should be doubled because only half of the traveling route is considered.

$$V = 2\int_0^T Avdt \tag{3.11}$$

In this case, we need to perform integration by parts. Therefore, we can express it in the following form:

$$V = 2v(\int_0^{t_0} A_{complete}dt + \int_{t_0}^{T} A_{incomplete}dt) \tag{3.12}$$

At $t = t_0$, $\overline{BD}$ is equivalent to the difference between the radii of the two circles, and at $t = T$, it is equivalent to the sum of the radii. Their expressions are shown in Equation 3.13 and Equation 3.14.

$$2Rsin(\frac{\omega t_0}{2}) = |r_j - r_h| \tag{3.13}$$

$$2Rsin(\frac{\omega T}{2}) = r_j + r_h \tag{3.14}$$

After the arrangement, t_0 and T can be determine as following

$$t_0 = \frac{2}{\omega}sin^{-1}(\frac{|r_j - r_h|}{2R}) \tag{3.15}$$

$$T = \frac{2}{\omega}sin^{-1}(\frac{r_j + r_h}{2R}) \tag{3.16}$$

After knowing the volume, the applied kinetic energy (KE) of a water slug can be determined according to Equation 3.2.

$$KE = \frac{1}{2}\rho_L V v^2 \tag{3.17}$$

Finally, the equivalent velocity is obtained for further analysis.

$$v_{eq} = \sqrt{\frac{2KE}{m_{ref}}} \tag{3.18}$$

3.4. Lifetime modeling of PA and PD

The Springer's equation (Equation 2.7) can be visualized in the form of a plot, as shown in Figure 3.9. The plot represents the number of impacts until the incubation period (n_i) vs. the ratio of the strength parameter to impact pressure ($\frac{S}{P}$) , with both axes on a logarithmic scale. The lower (Equation 2.9) and upper limits (Equation 2.10) are also shown in Figure 3.9. After obtaining experimental results that correlate velocity with the number of impacts, the velocity is then converted to $\frac{S}{P}$ for comparison with Springer's equation. By substituting the parameters of the coating and water material properties in Equation 2.2 and Equation 2.8, and by inserting different v_{eq} and v values, the corresponding n_i for $\frac{S}{P}$ can be determined. These data can then be plotted on Figure 3.9. This analysis aims to assess how the experimental results fit Springer's equation, in order to evaluate the validity of the model for both PA and PD coatings.

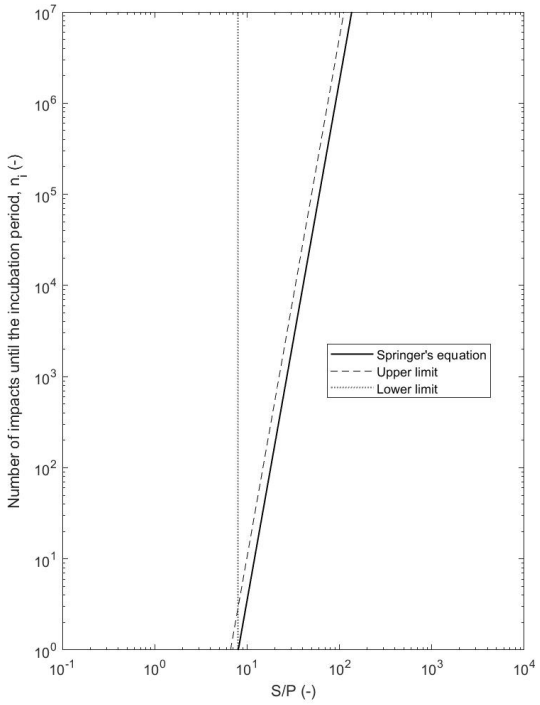

Figure 3.9: Number of impacts until the incubation period vs. $\frac{S}{P}$

The projected lifetime of PA and PD coatings was also determined using Verma's long-term rain erosion model (as discussed in subsection 2.7.2). According to different coatings, the inputs in the model should be modified including the coating properties (density (ρ_C), speed of sound (C_C), ultimate tensile strength (σ_U), and Poisson's ratio (ν)) and the Wöhler slope (m) obtained from the PJET as described in section 2.6. The other settings of the model were fixed. The coastal site of Wilhelminadorp (shown in Figure 3.10) was chosen for the meteorological data of the probabilistic rain model and the wind statistics model, considering the higher severity of erosion in this coastal area compared to inland areas [55]. The DTU 10-MW wind turbine was utilized in the wind turbine model, with its power curve and necessary specifications presented in Figure 3.11.

Additionally, the sensitivity of the lifetime prediction of this model to variations in material properties was studied, particularly, ultimate tensile strength (σ_U) and Poisson's ratio (ν). σ_U and ν are systematically varied within a range of 70% to 130% of their original values in Table 3.1, with 10% intervals, to evaluate their impact on the life prediction model. σ_U and ν are modified individually while keeping all other parameters constant. The resulting data is then represented using bar charts, with the same scale, to compare the sensitivity of the lifetime of PA and PD coatings at different Wöhler slopes (based on v

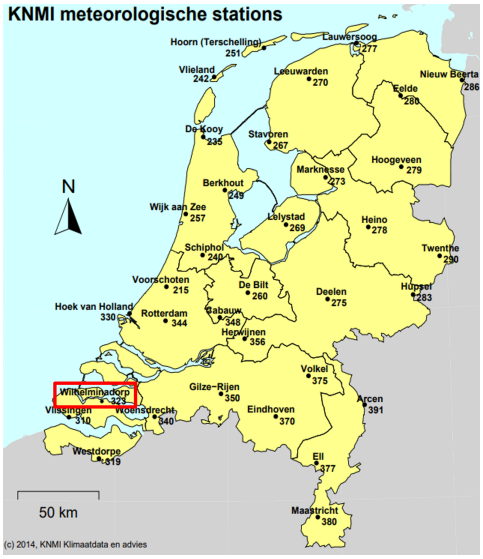

Figure 3.10: Cite considered for the lifetime prediction [32].

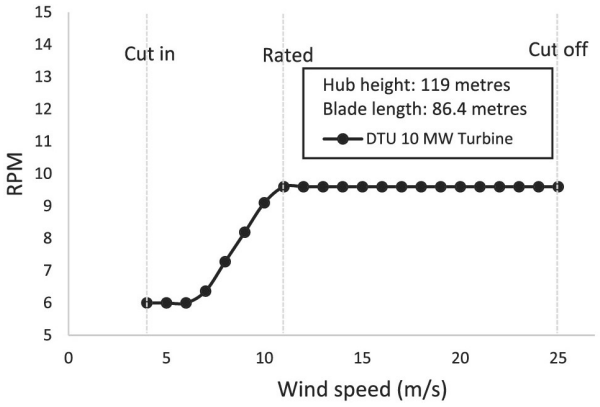

Figure 3.11: Power curve of the DTU 10-MW wind turbine [55].

or v_{eq}) to variations in σ_U and ν. This analysis provides insights into the influence of these material properties on the predicted lifespan of the coatings.

4

Results and discussion

This chapter offers the results and discussion of findings based on chapter 3. It begins by analyzing the concept of equivalent velocity in section 4.1, demonstrating the improvement of the water slug volume calculation and the interpretation of experimental results from the PJET. Section 4.2 focuses on the rain erosion experiment, presenting the number of impacts until the incubation period and the breakthrough and the surface damage evaluation. Finally, in section 4.3, the lifetime prediction of the coatings is evaluated using the leading-edge erosion model, providing insights into the feasibility of the model and the sensitivity of the material properties.

4.1. Correction for the volume interdependence by equivalent velocity

A comparison can be made between the theoretical volume calculation based on the proposed method and the calculation based on the assumption of a cylindrical water column. Table 4.1 displays the theoretical volumes of a single water droplet passing through the hole in the PJET facility, while the data in Table 4.2 is determined by assuming the water slug is a cylindrical column for a given overlap time of the hole and the water jet. Given the same impact velocity and impact frequency, the theoretical value is lower than the cylinder-based value. For instance, at an impact frequency (f) of 42 Hz and v = 160 $\frac{m}{s}$, the theoretical volume is accurately determined to be 184.8 mm^3, while the volume of the cylindrical water slug is 435.4 mm^3. The reason is that the cross-sectional area of the water slug fluctuates with time and reaches a maximum only when the area of the hole and the jet entirely overlap, whereas the cross-sectional area remains constant with this maximum value for the cylindrical column. Thus, it is concluded that the assumption of a cylindrical shape for a given overlap interval overestimates the amount of water that hits the sample by 2.36 times. Thus, the variation in the overlap region between the hole and the water jet affecting the volume of the slug should be taken into account.

Table 4.1: Theoretical volume calculation of a water slug in the PJET facility. (unit: mm^3)

v ($\frac{m}{s}$) \ f (Hz)	5	25	42
10	97.0	19.4	11.6
160	1552.2	310.4	184.8
250	2425.4	485.1	288.7

Table 4.2: Volume of a water slug assuming a cylindrical shape with the overlap time of the hole on the rotational disc and the water jet. (unit: mm^3)

v ($\frac{m}{s}$) \ f (Hz)	5	25	42
10	228.6	45.7	27.2
160	3657.6	731.5	435.4
250	5715.1	1143.0	680.4

The experimental data from previous research [14] is employed to compare the analyses using the conventional impact velocity (v) and proposed equivalent velocity (v_{eq}). The relation between v_{eq} and v for three different impact frequencies (2.5, 27.7, and 42.6 Hz) is depicted in Figure 4.1. The equation of power fit curves shows that v_{eq} is proportional to $v^{1.5}$. Looking at the first term of each fitted equation, the variation between v_{eq} and v increases as the impact frequency decreases.

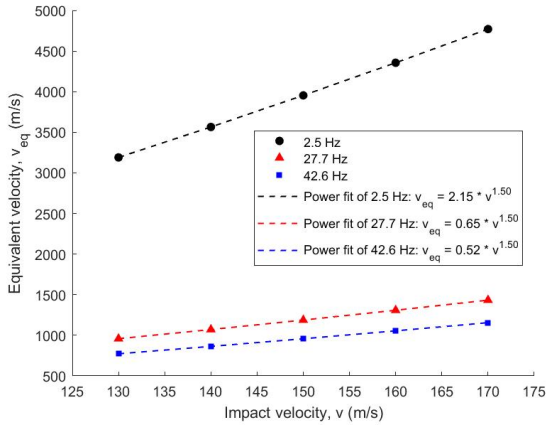

Figure 4.1: Relation between equivalent velocities and the impact velocities when the impact frequencies are 2.5 Hz, 27.7 Hz, and 42.6 Hz.

The result of $v_{eq} - n_i$ curve (new method) is shown in Figure 4.2b in comparison with the $v - n_i$ curve (old method) in Figure 4.2a. It is obvious that the positions of the three curves are reversed. In Figure 4.2b, the curve of 2.5 Hz shifts all the way to the top, while the curve of 42.6 Hz situates on the bottom. This implies that for the same size of the droplet at the same equivalent velocity, the higher the impact frequency the fewer the number of droplets needed to cause damage. This observation aligns with the expectation of the recovery of deformation and viscoelastic behavior: as the impact frequency increases, the polyurethane coating has less time to recover from the strain, leading to faster erosion.

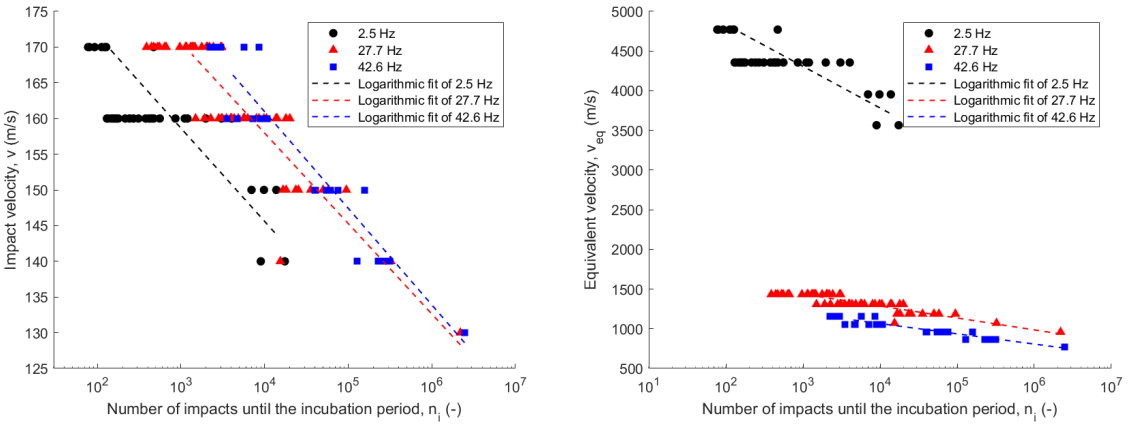

(a) $v - n_i$ curve. Adjusted from [14]

(b) $v_{eq} - ni$ curve

Figure 4.2: Result of the erosion of the polyurethane coating using water-jet rig presented by the impact velocity and equivalent velocity.

Table 4.3 shows that the Wöhler slopes (m) of the new method at three impact frequencies decrease significantly by 7 to 10 and become similar at around 18, indicating the sensitivity of the number of impacts to speed is higher in $v - n_i$ curve than in $v_{eq} - n_i$ curve. This less drastic change in the number of impacts in terms of the variation of v_{eq} reveals the alleviation of the impact velocity-volume dependency which high v leads to even smaller n_i with the synergy of a longer water slug. Additionally, the values of the Wöhler slope are consistent for the same material, suggesting a relatively predictable behavior of the material.

Table 4.3: Slopes of the $v - n_i$ curve and the $v_{eq} - n_i$ curve corresponding to three impact frequencies.

f (Hz)	2.5	27.7	42.6
m (-, $v - n_i$)	28.09	28.85	24.26
m (-, $v_{eq} - n_i$)	18.73	18.88	17.23

Overall, using the equivalent velocity to build the plot reduces the water slug volume interdependence with impact velocity and impact frequency when we present the result by velocity-number of impacts relationship.

4.2. Rain erosion experiments

In this section, the result of the rain erosion experiment is presented in parts. First, the measurements until the incubation period and the breakthrough are shown by number and erosion images. Furthermore, the erosion progression of mass loss and damaged area over time is analyzed, offering information about the erosion rate and microscopic observation.

4.2.1. Incubation period

The outcome of the incubation tests is illustrated by the impact velocity and the equivalent velocity in relation to the number of impacts until the incubation period in Figure 4.3. According to Equation 2.5, the curves presenting the power law relation can be written as

$$n_i = kv^{-m} \tag{4.1}$$

$$n_i = kv_{eq}^{-m} \tag{4.2}$$

where the fitted constants are displayed in Table 4.4. The trend of the decreasing number of impacts with the increasing velocity is observed for both PA and PD. Two figures show a similar pattern with the same n_i but the scale of v_{eq} is higher than that of v. The trend line of PA is steeper than that of PD, intersecting at around $v = 151\ \frac{m}{s}$ and $v_{eq} = 976\ \frac{m}{s}$. In the investigation of velocities higher than this crossover point, the PA exhibits a greater number of impacts until the incubation period compared to PD. Conversely, at lower impact velocities, PD demonstrates improved performance. Due to the relatively mild steepness of the curve for PD, it is deduced that PD has longer lifetimes for LEP on the wind turbine blades as the impact velocity is typically below 120 $\frac{m}{s}$ [4].

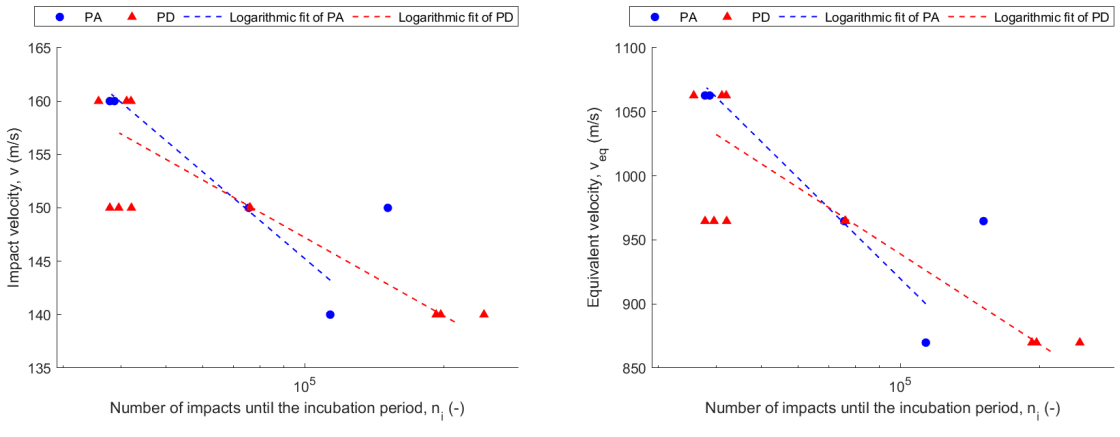

(a) $v - n_i$ curve **(b)** $v_{eq} - n_i$ curve

Figure 4.3: Performance of PA and PD presented by the impact velocity and equivalent velocity with respect to the number of impacts until the incubation period.

Table 4.4: Fitted constants for the curves.

	PA ($v - n_i$)	PD($v - n_i$)	PA($v_{eq} - n_i$)	PD ($v_{eq} - n_i$)
k	3×10^{22}	2×10^{32}	10^{21}	9×10^{29}
m	8.11	12.61	5.41	8.41

By applying the equivalent velocity scheme, the curves become steeper and are shifted upward compared to the old method. Due to different Wöhler slopes (m) and the order(s) of magnitude difference of k, a point of intersection for the $v - n_i$ curve and the $v_{eq} - n_i$ curve of each coating at a low velocity should be expected as both curves are extrapolated in one plot. This can be attributed to the concept of equivalent velocity, wherein a reference droplet's kinetic energy during travel is equated to the kinetic energy of a water slug moving at a specific velocity. When the impact velocity is high, the water slug's volume increases, resulting in a rise in kinetic energy. Conversely, at lower impact velocities, the water slug's volume decreases. At a certain impact velocity, the PJET generates a water slug volume equivalent to that of the reference droplet, which, in this case, is a spherical droplet with a diameter of 2 mm. Consequently, the equivalent velocity must be identical to the impact velocity to match the kinetic energy. If the impact velocity falls below this value, the 2 mm droplet is larger than the water slug, necessitating an equivalent velocity lower than the impact velocity.

To obtain the impact velocity leading to the same volume of the reference droplet, the following equation can be solved:

$$2v(\int_0^{t_0} A_{complete}dt + \int_{t_0}^{T} A_{incomplete}dt) = \frac{1}{6}\pi d^3 \tag{4.3}$$

where the left-hand side is the water slug's volume created by the PJET from Equation 3.12 and the right-hand side is the spherical volume of the reference droplet. Rearranging the equation, we can obtain the expression:

$$v = \frac{\pi d^3}{12(\int_0^{t_0} A_{complete}dt + \int_{t_0}^{T} A_{incomplete}dt)} \tag{4.4}$$

The calculation in this scenario considers an impact frequency of 42 Hz and a droplet size of 2 mm. The impact velocity required to generate a water slug's volume equivalent to that of the 2 mm reference droplet is calculated to be 3.6 $\frac{m}{s}$.

Extrapolating the $v - n_i$ curve and $v_{eq} - n_i$ curve of PA and PD, the crossover point for PA is at 3.5 $\frac{m}{s}$, and that for PD is at 3.6 $\frac{m}{s}$. These crossover points match the calculation quite well. Within the impact velocity regimes of most operating wind turbines (from 60 to 100 $\frac{m}{s}$ [60]), a higher number of impacts is expected for the new method (in Figure 4.3b) than the old method (in Figure 4.3a). However, when the impact velocity of 2 mm droplets is lower than 3.6 $\frac{m}{s}$, fewer impacts are needed to damage the coating compared to the interpretation of the $v - n_i$ curve. This usually happens only at some times when wind turbines are not in operation because the impact velocity is very slow.

At $v = 160\,\frac{m}{s}$, the average number of impacts until the incubation period of PA and PD is very close and the range of all measurements is narrow. The scatter of the measurements at $v = 150\,\frac{m}{s}$ is significant for both materials. The minimum measured number of impacts of PA is nearly the same as that of the maximum of PD. Yet, their average values are distinct. Therefore, the p value is an indicator to show whether the number of impacts can be considered statistically different. If the p value is lower than the significance level of 0.05, the null hypothesis, which states that the two groups of measurements have equal means, is rejected. As a result, there is a significant difference in the two mean numbers of impacts. According to Table 4.5, the p values for the group of $v = 150\,\frac{m}{s}$ and $v = 160\,\frac{m}{s}$ are larger than the significant level of 0.05, indicating there is no significant difference in the incubation periods between PA and PD at these velocities. In contrast, a significant variation is found for the impact velocity of $140\,\frac{m}{s}$, where the p value is below 0.05. This finding further supports the previous deduction that the incubation period for PD is longer than that for PA as the velocity decreases.

Table 4.5: p values for the measurements of PA and the measurements of PD under the same impact velocity.

Impact velocity ($\frac{m}{s}$)	p value	Significant difference
140	0.012	Yes
150	0.077	No
160	0.48	No

Another type of p values indicating whether the number of impacts at different velocities varies markedly considering the same coating, as shown in Table 4.6. For PA, the number of impacts does not have a substantial change per $10\ \frac{m}{s}$, while there is a significant difference between the measurements at $v = 160\ \frac{m}{s}$ and $v = 140\ \frac{m}{s}$. For PD, the difference between $v = 160\ \frac{m}{s}$ and $v = 150\ \frac{m}{s}$ is small, but the distinction is found at $v = 140\ \frac{m}{s}$. The incubation test results at high velocities ($v = 150\ \frac{m}{s}$ and $v = 160\ \frac{m}{s}$) show little variation in the number of impacts for both coatings.

Table 4.6: Pairwise p values between different impact velocity groups.

Impact velocity groups ($\frac{m}{s}$)	PA		PD	
	p value	Significant difference	p value	Significant difference
140 vs. 150	0.54	No	<0.001	Yes
150 vs. 160	0.053	No	0.27	No
140 vs. 160	<0.001	Yes	<0.001	Yes

The initial damage until the incubation period is investigated via the 3D microscope as shown in Figure 4.4. It is apparent that the damage for PD is more severe than for PA. The failure mode for PA is mainly pitting. The damage consists of a few dents close by within a circle of 4.5 mm in diameter. The total damaged area is between 0.7 to 1.2 mm^2. The damage characteristic does not vary with three different velocities. On the other hand, relatively large craters can be observed on the surface of PD. The predominant failure mode is cratering. The damaged area tends to grow with increasing velocity. The damaged areas are 5.7, 6.6, and 37.3 mm^2 at 140, 150, and 160 $\frac{m}{s}$ respectively.

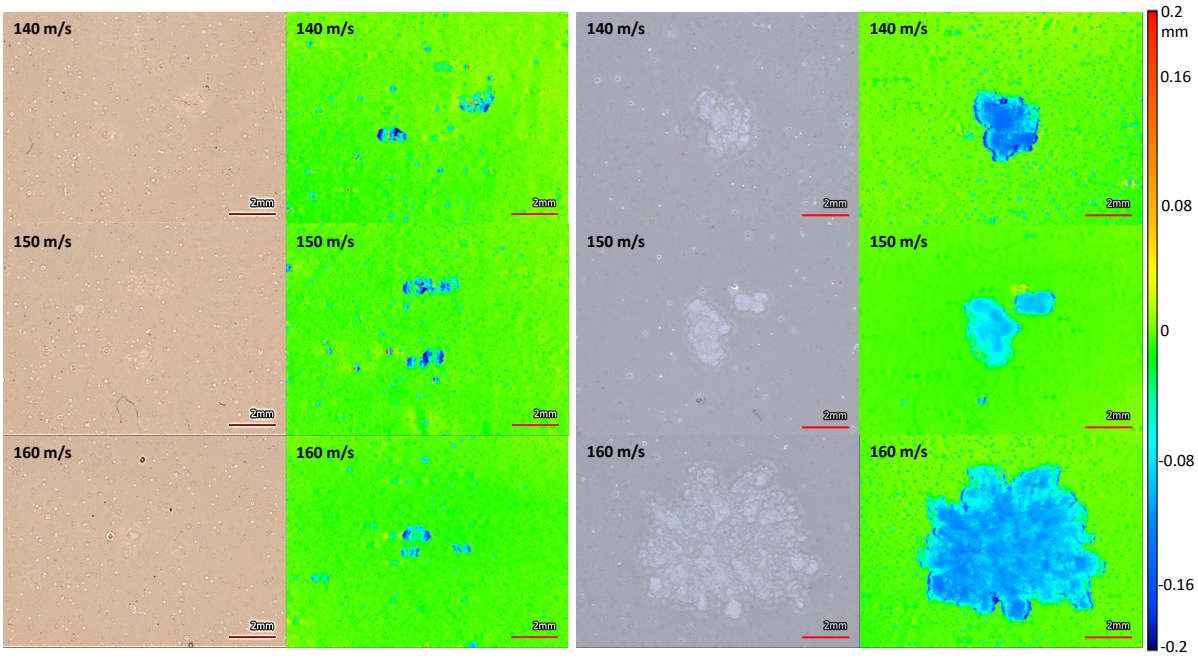

(a) PA **(b)** PD

Figure 4.4: Optical images and height maps showing the surface damage until the incubation period.

4.2.2. Breakthrough

After the test for the incubation period, the results of the breakthrough are demonstrated in the section. Figure 4.5 presents the performance of PA and PD by the erosion test until breakthrough. Similar to the incubation, the average number of impacts increases as the velocity drops. The power law relation can again be written as

$$n_b = kv^{-m} \tag{4.5}$$

$$n_b = kv_{eq}^{-m} \tag{4.6}$$

where the fitted constants based upon these averaged points are shown in Table 4.7. In contrast to the incubation period, PA coatings exhibit higher k and m values compared to PD coatings. However, in Figure 4.5, PD requires 2 to 3 times more impacts on average than PA to reach the breakthrough at the same velocity. By considering the results of the incubation period in Figure 4.3 and the breakthrough in Figure 4.5 at the same velocity (a tabular comparison is in Appendix A), it is observed that the erosion time until the breakthrough is 3 to 4 times longer than the incubation period for PA coatings. For PD coatings, the erosion time until the breakthrough is more than 10 times longer than the incubation period.

Besides, the point of intersection does not appear in Figure 4.5. It would be located at $v = 126\ \frac{m}{s}$ and $v_{eq} = 737\ \frac{m}{s}$ if two curves were extrapolated. Below the point of intersection, the PA demonstrates a greater number of impacts until the breakthrough compared to PD at the same velocity. This implies that the lifetime in terms of the breakthrough is higher for PA than PD undergoing real-life impact velocities. This finding, in conjunction with the results from the incubation test, indicates that PD has a longer incubation period but reaches the breakthrough faster, whereas stiffer materials like PA may offer better resistance against the breakthrough in the low-velocity range. However, further verification under low-velocity testing is required to substantiate these observations.

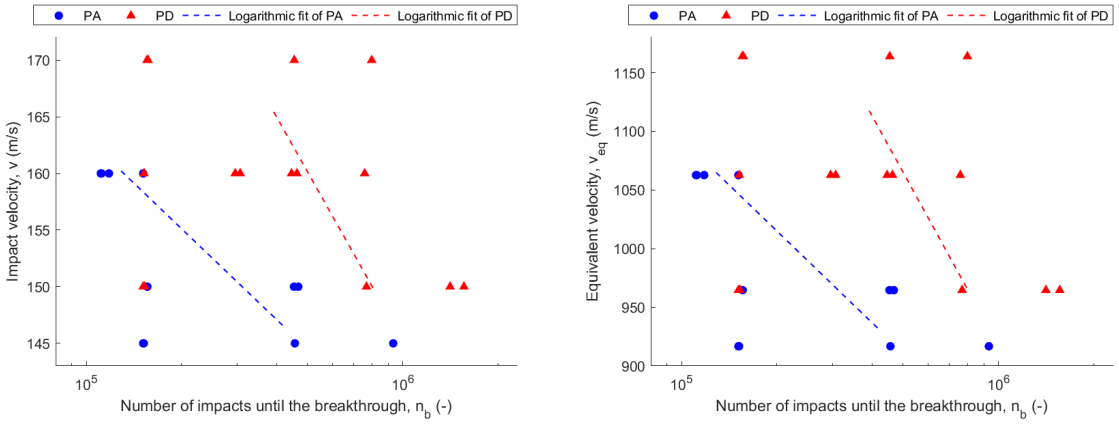

(a) $v - n_b$ curve **(b)** $v_{eq} - n_b$ curve

Figure 4.5: Performance of PA and PD presented by the impact velocity and equivalent velocity with respect to the number of impacts until the breakthrough.

Table 4.7: Fitted constants for the curves.

	PA $(v - n_b)$	PD$(v - n_b)$	PA$(v_{eq} - n_b)$	PD $(v_{eq} - n_b)$
k	7×10^{32}	4×10^{18}	3×10^{30}	3×10^{17}
m	12.59	5.86	8.39	3.91

It is also observed that the trend lines are steeper and shifted upward after converting the $v - n_b$ curve to the $v_{eq} - n_b$ curve. Extrapolating both curves toward lower velocities, we would expect a point of intersection for each coating in one plot. For PA, this intersection point occurs at 57 $\frac{m}{s}$, while for PD,

it occurs at 59 $\frac{m}{s}$. The utilization of the reference droplet (2 mm sphere) and the PJET's water slug at these two velocities gives the same number of impacts until the breakthrough for PA and PD. However, if the velocity surpasses these values, the number of impacts from $v_{eq} - n_b$ curves is larger than that from $v - n_b$ curves, whereas $v_{eq} - n_b$ curves show smaller n_b when the velocity falls below these values. Two points are below the impact velocity regime encountered in operating wind turbines, but they are not as low as the previously calculated expected point of intersection at 3.6 $\frac{m}{s}$. This discrepancy is likely due to the fitting of curves based on scattered measurements.

Another attention is paid to the scatter of each measurement. Despite excluding outliers, substantial variability within the data is seen. A notable observation is the range of measurements for PD, particularly at $v = 150\ \frac{m}{s}$, indicated by a substantial 10-fold difference between the maximum and minimum number of impacts until the breakthrough. This wide range encompasses the entire range of measurements observed for PA at the same velocity. This aligns with the p value 0.31 shown in Table 4.8 that the difference in the average number of impacts between PA and PD at $v = 150\ \frac{m}{s}$ is insignificant. This variability could be attributed to manufacturing defects of samples such as voids. On the other hand, there is evidence supporting the superior performance of PD compared to PA at the impact velocity of 160 $\frac{m}{s}$ since the p value falls below 0.05.

Table 4.8: p values for the measurements of PA and the measurements of PD under the same impact velocity.

Impact velocity ($\frac{m}{s}$)	p value	Significant difference
150	0.31	No
160	0.033	Yes

Moreover, all mean numbers of impacts of different velocity groups are not markedly different for both materials, except the p value is lower than the significant level of 0.05 between the PA's measurements at $v = 150\ \frac{m}{s}$ and $v = 160\ \frac{m}{s}$ as displayed in Table 4.9. For PD, the ranges of the number of impacts at three velocities largely overlap. As a result, all p values in Table 4.10 are greater than 0.05 comparing all the measurements tested at three different velocities. This implies that the statistical result does not provide strong evidence supporting the trend of decreasing impact velocity leading to an increasing number of impacts for PD. Therefore, conducting experiments at a wider range of velocities is necessary to provide a more comprehensive view of the relationship between the number of impacts and impact velocity.

Table 4.9: Pairwise p values between different impact velocity groups for PA.

Impact velocity groups ($\frac{m}{s}$)	PA	
	p value	Significant difference
145 vs. 150	0.80	No
150 vs. 160	0.022	Yes
145 vs. 160	0.112	No

Table 4.10: Pairwise p values between different impact velocity groups for PD.

Impact velocity groups ($\frac{m}{s}$)	PD	
	p value	Significant difference
150 vs. 160	0.23	No
160 vs. 170	0.98	No
150 vs. 170	0.29	No

The samples were observed after the erosion. Figure 4.6 displays the representative surface damage until the breakthrough at selected impact velocities for PA and PD. All damages until the breakthrough are obvious since the coating layer was penetrated. The main failure mode is pitting for PA and cratering for PD. The damaged areas of PA vary from 4 to 100 mm^2 regardless of the impact velocity. In contrast, the damaged areas measured among the PD's test spots are more consistent, from 38 to 85 mm^2. In addition, there are other characteristics found as presented in Figure 4.7. Debonding is seen on several PA surfaces, particularly at high-impact velocities (150 and 160 $\frac{m}{s}$), and some of them appear with peeling and cracks on the coating. However, these damage characteristics are not seen in PD. Only crater-like damage is observed on the coating, but further pitting and cracks on the filler occurred on some test spots. This damage underneath the coating layer is not studied in this research.

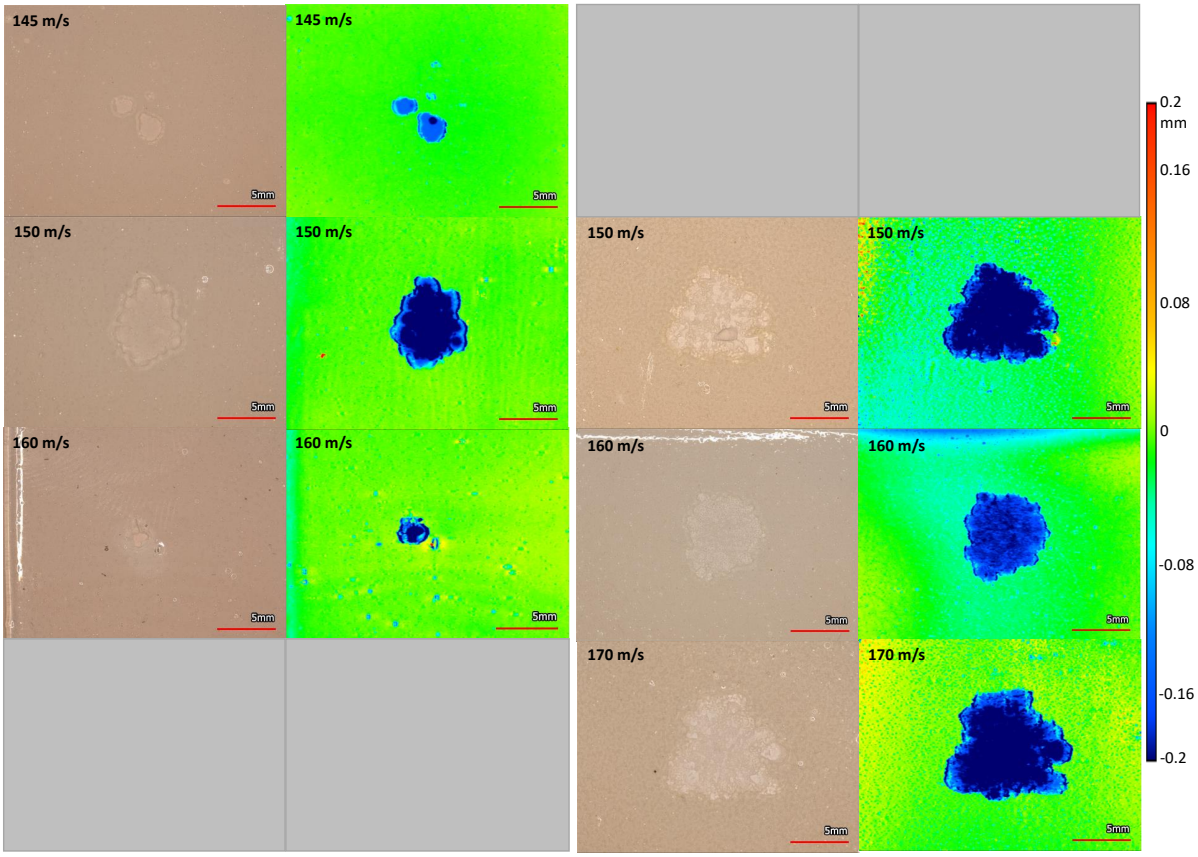

(a) PA **(b)** PD

Figure 4.6: Optical images and height maps showing the surface damage until the breakthrough.

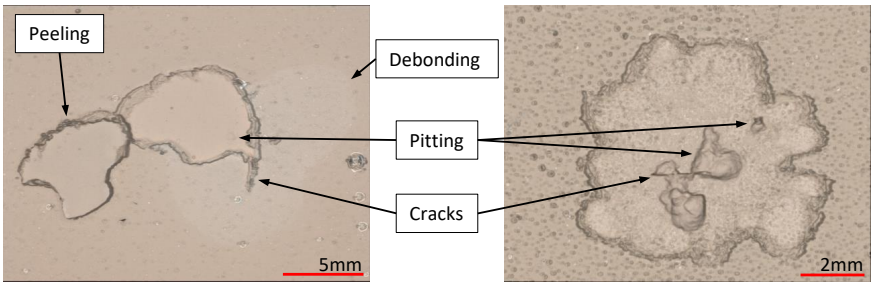

Figure 4.7: Damage characteristics of (a) PA at v =150 $\frac{m}{s}$ and (b) PD at v =170 $\frac{m}{s}$.

4.2.3. Erosion progression

After analyzing the damage progression during the incubation period and breakthrough, we also conducted a few tests in between them to investigate the cumulative erosion process for both PA and PD coatings. These tests were performed at an impact velocity of 160 $\frac{m}{s}$, which corresponds to the available data for incubation and breakthrough, and where distinct mean breakthrough measurements were obtained, as shown in Table 4.8. Their results are presented in Figure 4.8, which depicts the erosion graph illustrating the progression of mass loss over the testing duration and damaged area over the testing duration. Examples of microscopic surface erosion corresponding to each testing interval are shown in Figure 4.9.

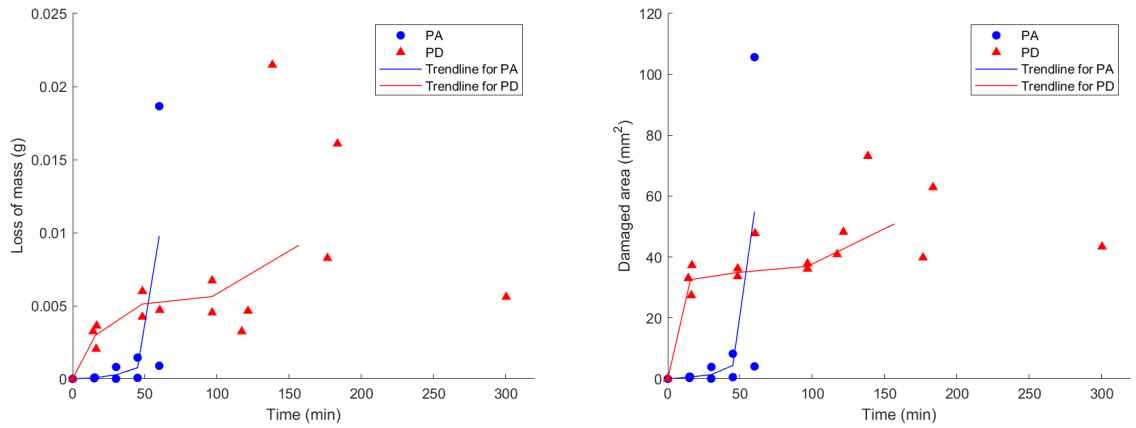

(a) Loss of mass vs. time

(b) Damaged area vs. time

Figure 4.8: Erosion graph until the breakthrough of PA and PD at $v = 160 \frac{m}{s}$.

The erosion progression observed for PA and PD coatings exhibit distinct characteristics in Figure 4.8. For PA, shown in Figure 4.8a, mild damage occurs within a short time span of 50 minutes, followed by a significant increase in the average mass loss from less than 0.001 to nearly 0.01 grams in the subsequent 15 minutes, corresponding to the breakthrough. This phenomenon can also be observed from Figure 4.9a, where the surface damage starts with mild pitting, advances to gouges, and eventually leads to an obvious loss of material and debonding until the breakthrough. The trend for the damaged area over the erosion time of PA in Figure 4.8b is similar to its mass loss progression in Figure 4.8a, implying the growth of damage is attributed to both the thickness and area.

On the other hand, PD demonstrates a more gradual mass loss throughout the entire erosion progression in Figure 4.8a. Nevertheless, the size of the damaged area tends to stabilize at around 45 mm^2 after the incubation period as shown in Figure 4.8b. This trend is also evident in Figure 4.9b, where a substantial crater is observed initially and its size remains relatively unchanged until the breakthrough. Hence, it highlights that the growth of damage in PD is mostly through thickness after the initial damage appears.

The total mass losses until the breakthrough are approximately the same (0.01 grams) for both PA and PD coatings although the damaged topography differs between the two. Despite the fact that the damaged area of PD is greater than that of PA, as evident from the darkest blue region in the height map, the extent of PD eroded down to the filler material is tiny, whereas a considerably larger area of PA has eroded to the filler.

In the aspect of surface morphology, PA exhibits higher mass loss per unit area compared to PD. This may imply that the erosion mechanisms of the two materials differ. Based on the observed large area of damage, it is reasonable to deduce that lateral jetting plays a significant role in the erosion of PD. This can be attributed to its low Young's modulus, which allows water to deform the material and pave the way for lateral jetting. In contrast, the stiff property of PA results in pitting characteristics on its surface, which may be caused by the water hammer pressure and stress waves rather than lateral jetting. The damage in PA seems to mainly occur in localized areas, while the surrounding material remains relatively undisturbed. Over time, the pits on PA's surface grow and merge, leading to a larger area of damage until the breakthrough. However, only the failures that involve debonding and peeling, as shown in Figure 4.7, demonstrate the evident influence of lateral jetting. Additionally, the ductile nature of PD contributes to a more gradual loss of mass during the erosion process. The material's ability to dissipate the impact over a broader region helps reduce the severity of damage in any single localized area. From the experimental point of view, Young's modulus might be a key factor in the erosion resistance as the other properties of PA and PD are quite similar in Table 3.1.

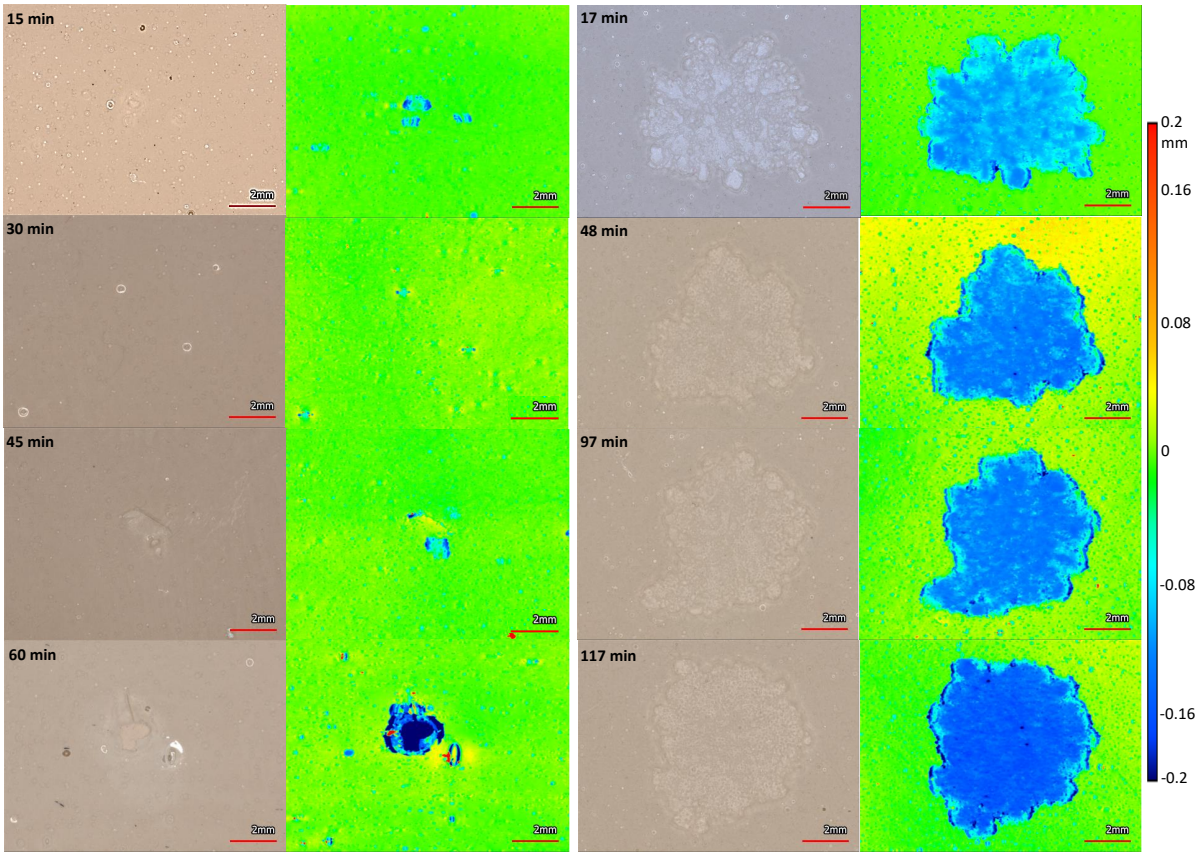

(a) PA **(b)** PD

Figure 4.9: Microscopic images of mass loss progression of (a) PA and (b) PD at $v = 160 \frac{m}{s}$. Images from top to bottom show progressive surface erosion from the incubation period to the breakthrough.

4.3. Lifetime prediction by leading-edge erosion model

In this section, the lifetime prediction of the PA and PD is discussed using the leading-edge erosion model. The lifetimes predicted by the model are displayed and discussed. In addition, a sensitivity analysis of the model is provided, which investigates the implications of differences in ultimate tensile strength and Poisson's ratio on expected lifetimes.

4.3.1. Lifetime of PA and PD

We now focus on the lifetime prediction of the PA and PD coatings using the long-term leading edge erosion model based on the experimental data. The results of the lifetime predictions are presented in Table 4.11. Based on the Wöhler slope (m) from the $v - n_i$ curve (old method) and the $v_{eq} - n_i$ curve (new method), two different expressions are considered. The lifetimes (t), expressed in years, are shown in the respective columns.

Table 4.11: Lifetime prediction of PA and PD. (unit: years)

	t (m from $v - n_i$)	t (m from $v_{eq} - n_i$)
PA	8.40×10^{-9}	5.49×10^{-10}
PD	4.16×10^{-8}	3.21×10^{-9}

Comparing PA and PD, the expected lifetime of the PA under long-term leading edge erosion conditions is shorter than that of PD, which aligns with the previous discussion in 4.2.1 if a real-life situation is considered. Nonetheless, these values are extremely small. Converting them to seconds, none of them is

higher than 1.5 seconds. These predictions are neither close to the normal lifetimes of the coatings nor the experimental results. Additionally, the lifetime in the case of $v_{eq} - n_i$ curve should be expected to be higher in comparison with the $v - n_i$ curve since the number of impacts until the incubation period is higher for most of the velocity regime (when velocity is above 3.6 $\frac{m}{s}$) as discussed in subsection 4.2.1. However, the opposite results are discovered.

As a result, it is essential to examine the feasibility of Springer's model in predicting the performance of PA and PD. First of all, the measurements plotted in comparison with Springer's equation (solid line) are shown in Figure 4.10. Each data point represents a single measurement until the incubation period as indicated in Table 3.4. n_i is taken from the test results. S is calculated using Equation 2.8 with σ_U and ν from Table 3.1 and m from Table 4.4. To calculate P (Equation 2.2), ρ_C and C_C are from Table 3.1, as well as the density of water (ρ_L) and the speed of sound in water (C_L) are assumed to be 1000 $\frac{kg}{m^3}$ and 1480 $\frac{m}{s}$, respectively. Due to vertical impingements, $cos\theta$ is 1. The velocity input corresponds to either the impact velocity (v) or the equivalent velocity (v_{eq}).

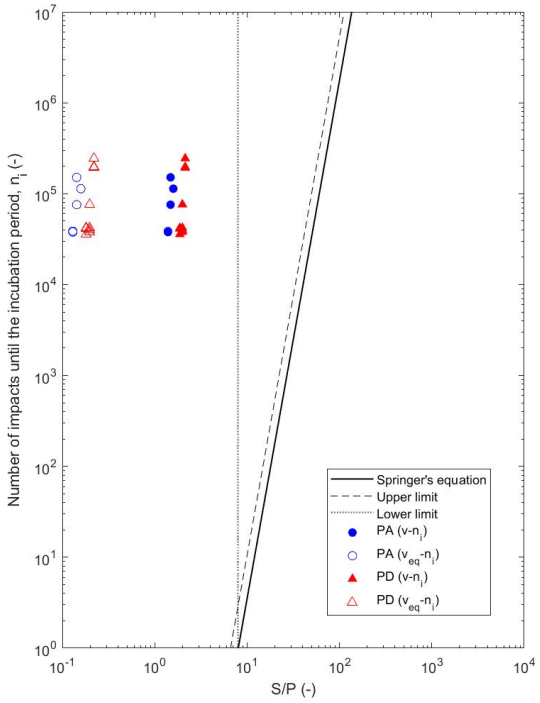

Figure 4.10: Experimental data of the incubation tests plotted in comparison with Springer's equation. Fitted equations of the data points can be found in Appendix B.

This discrepancy between the experimental data points and Springer's equation shed light on the underestimation of lifetime prediction in Table 4.11. If the data points of the old method and new method are extrapolated to the right (toward the lower impact velocities of most operating wind turbines), n_i is higher at the same value of $\frac{S}{P}$ compared with Springer's equation.

When examining the data points of the old method in Figure 4.10, a leftward shift away from Springer's equation is observed. Moreover, an even more drastic leftward shift is found in the data points of the new method, which are shifted approximately one order of magnitude further away from the old method. This phenomenon can be attributed to the small $\frac{S}{P}$ values, indicating small values for S and large values for P. It is suspected that the ultimate tensile strength (σ_U) has a predominate impact on the left shift, as the values given in Table 3.1 are significantly lower than what is typically observed in common polymers [11, 37, 47].

Comparing the old method with the new method, the differences in input parameters are the velocity and Wöhler slope. The equivalent velocity (v_{eq}) is much larger than the impact velocity (v), and m becomes smaller as replacing the old method with the new method. This explains why $v_{eq} - n_i$ data points are located to the left of the $v - n_i$ data points.

Furthermore, the limitations of Springer's model as shown in subsection 2.7.1 were checked. According to Equation 2.9, the ratio of the strength parameter to impact pressure ($\frac{S}{P}$) should be greater than 8 to meet the minimum requirement of at least one impact. This lower limit is indicated by the dotted line in Figure 4.10, and the data points are required to be located at the right-hand side of the line. Hence, all the measurements do not meet the lower limit. As regards the upper limit shown as a dashed line (Equation 2.10), the data points should not be above the line. Thus, the upper limit is not fulfilled either.

The last limitation assessed is whether the thickness of the coating is sufficient to disregard stress wave reflection. According to the Equation 2.11, the thicknesses of PA coating should be larger than

$$2 \times 2 \times \frac{1807}{1480} = 5.05 \text{ mm}$$

and PD should be thicker than

$$2 \times 2 \times \frac{1710}{1480} = 4.62 \text{ mm}$$

However, the coating thickness is only 0.25 mm on average, indicating that this assumption is not met for any of the data. Consequently, the number of impacts until the incubation period estimated by Springer's homogeneous model is expected to be higher than the actual values obtained in the experiments, as the model does not consider the influence of wave reflection that accelerate erosion. Yet, Figure 4.10 shows the opposite. Given the same value of $\frac{S}{P}$, Springer's curve yields a lower n_i. This implies that the violation of the lower and upper limits may have a larger impact on the lifetime prediction than the neglect of wave reflection.

In light of the uncertainty about the accuracy of the σ_U, the additional lifetime prediction altering the σ_U of the PD material to 65 MPa was investigated in Table 4.12. This σ_U is chosen based on the specification that falls within the range commonly observed in polymers [48]. Yet, we should keep in mind that rain erosion testers cause a high strain rate (above 10000 Hz) behavior of polymers [36], thus the exact material properties are still not fully understood.

Table 4.12: Lifetime prediction of PD with the adjusted $\sigma_U = 65$ MPa. (unit: years)

	t (m from $v - n_i$)	t (m from $v_{eq} - n_i$)
PD ($\sigma_U = 65$ MPa)	13.62	1.05

Adjusting the ultimate tensile strength of the PD coating to 65 MPa yields significantly longer lifetimes. In this scenario, the PD coating is predicted to have a lifetime of approximately 13.62 years when using the old method and 1.05 years when using the new method. The results come close to the same order of magnitude as those in the literature [55]. Possible explanations for this discrepancy compared to the originally predicted lifetime could include the inability to measure properties at high strain rates and the presence of initial manufacturing defects. Therefore, the accuracy of material properties and the quality of the material are of importance in the rain erosion model.

In Figure 4.11, the old method fulfills the upper and lower limitations and fits well after altering the σ_U to a common value, whereas the new method remains a left shift, which can again be attributed to the smaller Wöhler slope value and much higher velocities. Consequently, it is deduced that the new method is not compatible with Springer's equation.

It can be argued that Springer's equation only considers m from the $v - n_i$, but k (in Table 4.4) which acts as a shifting factor and influences the curves significantly is excluded. However, the shifting of the

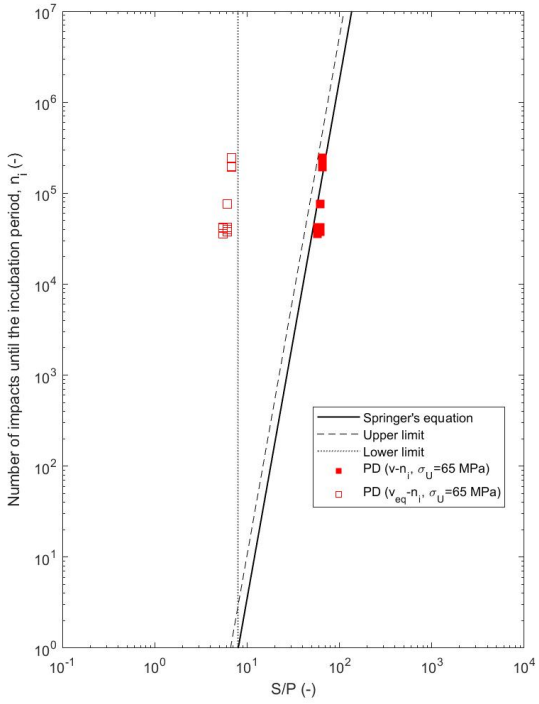

Figure 4.11: PD data with $\sigma_U = 65$ MPa plotted in comparison with Springer's equation. Fitted equations of the data points can be found in Appendix B.

traditional fatigue curve (stress vs. number of cycles) is associated with the σ_U which determines the y-intercept, and Springer's model already considers this parameter. Therefore, the k value should have a minor effect. On the other hand, the $v_{eq} - n_i$ curve is a modified expression of the $v - n_i$ curve, which means the further shifting can no longer be described by the σ_U. Hence, the model should be refined to adjust the change in the velocity level if the v_{eq} is employed in order to provide a better prediction for the new method.

The longer lifetimes and better fit for Springer's equation obtained by adjusting the ultimate tensile strength of the PD coating highlights the marked impact of material properties on the predicted lifespan of the coating. Hence, a sensitivity study of the long-term leading edge erosion model is demonstrated in the next subsection.

4.3.2. Sensitivity analysis

This study aims to evaluate the effects of varying Poisson's ratio (ν) and ultimate tensile strength (σ_U), the two largest influences of material properties [30], on the predicted lifespan. The results are presented graphically in Figure 4.12 and Figure 4.13.

Figure 4.12 illustrates the sensitivity of the lifetime predictions to variations in the ultimate tensile strength (σ_U) in the range of 70% to 130% of its original value. The graph clearly shows a consistent trend: as the ultimate tensile strength increases, the predicted lifespan of the coating also increases. This relationship holds true for both PA and PD coatings regardless of the opted m and σ_U. The change in lifespan is significant, with the lifetime varying by 1 to 2 orders of magnitude within a range of ±30%. This exponential relationship with a factor of 5.7, as described by the analytical equation (Equation 2.7).

Similarly, Figure 4.13 shows the sensitivity of Poisson's ratio on the lifetime. Again, the range for ν is 70% to 130% of its initial value. The graph also reveals that the higher the Poisson's ratio the longer

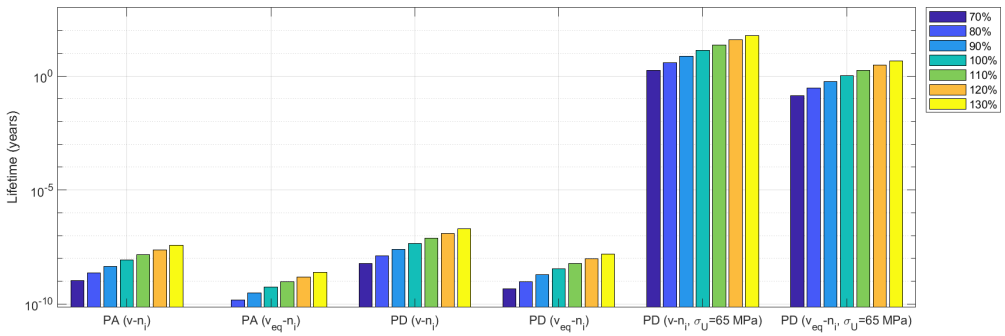

Figure 4.12: Lifetime sensitivity of variations in ultimate tensile strength (σ_U).

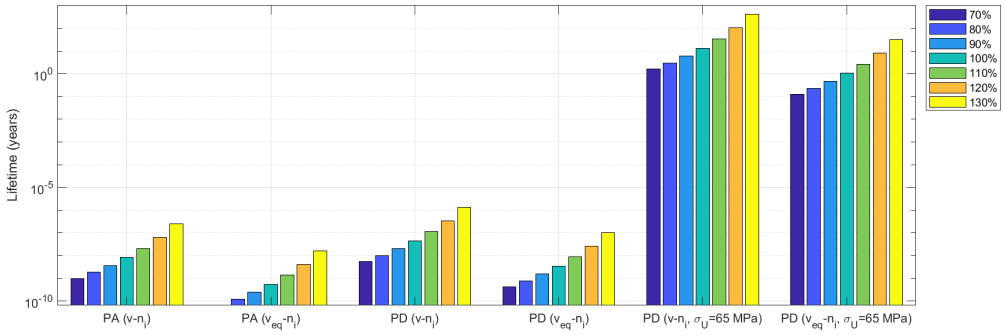

Figure 4.13: Lifetime sensitivity of variations in Poisson's ratio (ν).

the lifetime. The variation in lifetime is even more significant compared to the sensitivity to σ_U, with a variation of 2 to 3 orders of magnitude. For instance, in the case of PD ($v-n_i$, σ_U =65 MPa), increasing σ_U from 70% to 130% results in a lifetime increase from 1.78 to 60.74 years. On the other hand, an increase from 1.64 to 411.10 years is observed for the same range of the variation of ν.

The sensitivity analysis conducted in this study confirms the high sensitivity of lifetime predictions to changes in Poisson's ratio and ultimate tensile strength. The results indicate that materials with higher incompressibility ($\nu \rightarrow 0.5$) and higher ultimate tensile strength have longer projected lifetimes in the model. This analysis emphasizes the substantial influence of material properties on the coating's lifetime and the importance of accurate input material properties.

5

Conclusion

The purpose of this report was to propose a novel analysis method utilizing the concept of applied kinetic energy to address the issue of volume interdependence in the Pulsating Jet Erosion Test (PJET). In addition, rain erosion tests were carried out using the PJET to investigate the performance of two types of advanced polymer-coated samples, PA and PD, under different impact velocities. The lifespan of these samples was then predicted using the long-term rain erosion model. In the following discussion, the research questions outlined in section 2.8 are answered.

Research question 1: How does the relationship between impact velocity and the number of impacts until failure affect the interpretation of surface fatigue in PJET results, and what alternative method can better describe this surface fatigue?

The Pulsating Jet Erosion Test (PJET) generates water slugs with varying volumes due to different impact velocities and frequencies. This variability poses challenges in interpreting the experimental results presented by the conventional $v - n$ curve, which represents the impact velocity in relation to the number of impacts until failure. To address this issue, the concept of "equivalent velocity (v_{eq})" is introduced. v_{eq} is the velocity at which a spherical droplet should impact a surface to exert the same kinetic energy per impingement as the actual water slug traveling at the impact velocity (v). This approach allows for analysis using consistent droplet volumes while adjusting the velocity to maintain the same kinetic energy.

To determine the kinetic energy of a water slug, the volume of its irregular shape created by the PJET is crucial. This is achieved by dividing the overlap region between the jet and the hole into the complete overlap region and the incomplete overlap region. The volume is obtained by integrating the volumetric flow rate over time, taking into account both overlap regions. This calculation is called the theoretical volume calculation highlighting the consideration of the change in the overlap region over time. It demonstrates that the assumption of a cylindrical water slug used in previous research overestimates the volume by 2.36 times in comparison with the theoretical volume calculation.

The mass of the water slug is obtained by multiplying the volume by the density, allowing for the calculation of its kinetic energy as half of its mass multiplied by the square of the impact velocity. Subsequently, the equivalent velocity is determined by identifying the velocity at which a spherical droplet with a diameter of 2 mm possesses the same kinetic energy as the water slug.

At a constant impact frequency (f), the relationship between the equivalent velocity and the actual impact velocity follows a power law, where the equivalent velocity is proportional to the actual impact velocity raised to the power of 1.5. Comparing the representation of the $v - n$ curve and the $v_{eq} - n$ curve, the latter exhibits a steeper slope and shifts upward with an increase in velocity at the same number of impacts. This suggests a reduction in the impact velocity-volume dependency, indicating that more spherical droplets are required to cause damage at the same velocity. Moreover, the high-volume add-on effect resulting from the high-speed jet is corrected.

When v is held constant, a higher number of impacts is needed to initiate damage on the polymer coating at high f compared to low f. This observation suggests that the smaller droplet volume resulting from the high f by the PJET facility may hinder the effects of viscoelastic behavior where the relaxation time for recovery between each impact is shorter for high f. Conversely, implementing v_{eq} reveals a smaller number of impacts at higher f, consistent with the viscoelastic behavior where less recovery from deformation occurs.

In summary, this study suggests the concept of equivalent velocity to describe surface fatigue in the PJET. It mitigates the influence of the volume interdependence with impact velocity and frequency, providing a more comprehensive interpretation.

Research question 2: How do the PA and PD samples perform under the PJET in terms of the incubation period and the breakthrough?

The incubation period refers to the duration until the surface damage is observable and the breakthrough refers to the moment when the filler is exposed due to the loss of the coating above. In general, higher impact velocities tend to result in shorter incubation periods and lower numbers of impacts until breakthrough, following an inverse power law relationship. At high impact velocities (150 and 160 $\frac{m}{s}$), PA and PD exhibit similar performance in terms of the incubation period. However, at v =140 $\frac{m}{s}$, PD resists twice the number of impacts compared to PA. For the breakthrough, PD requires 2 to 3 times more impacts on average than PA at v =150 and 160 $\frac{m}{s}$. These findings suggest that materials with ductile characteristics, such as PD, demonstrate better resistance to rain erosion tests compared to stiffer materials like PA.

Analyzing the fitted Wöhler slope (m) based on the average number of impacts until the incubation period (n_i) with respect to the velocity reveals that PD has a larger slope compared to PA, resulting in a less steep $v - n_i$ curve. Two curves for PA and PD intersect within the test window at $v = 151\ \frac{m}{s}$ and $v_{eq} = 976\ \frac{m}{s}$. On the other hand, the curve for PD obtained from the breakthrough is steeper than the curve for PA, with an expected intersection point outside of the test window at $v = 126\ \frac{m}{s}$ and $v_{eq} = 737\ \frac{m}{s}$. Extrapolating both curves of the incubation period and the breakthrough to the common velocity regime of operating wind turbines, it can be concluded that the lifetime of PA, in terms of the incubation period, would still be shorter than that of PD. However, the lifetime of PA, in terms of the breakthrough, would be longer than PD. Nonetheless, the statistical results fail to provide strong evidence indicating a variation in the mean number of impacts until failure across different tested velocities. Therefore, the validity of the Wöhler slopes in this study cannot be assured.

Research question 3: How do PA and PD samples behave throughout the erosion progression until the breakthrough?

The erosion progression at an impact velocity of $160\ \frac{m}{s}$ until the breakthrough of PA and PD samples exhibits distinct characteristics. PA coating initially experiences a smaller erosion rate, followed by a significant increase in the loss of mass and the area of damage leading to the breakthrough. The main failure mode observed is pitting, likely caused by water hammer pressure and stress waves. The stiff nature of PA leads to localized areas of damage, which grow and merge over time until the breakthrough. In contrast, PD demonstrates a more gradual mass loss throughout the entire erosion progression, with the damaged area stabilizing after the incubation period. The growth of damage in PD is primarily through thickness. The presence of large crater damage can be attributed to the influential lateral jetting mechanism. The ductile nature of PD shows the ability to dissipate impact over a broader region, reducing the severity of damage in any single localized area. The investigation of erosion progression reveals the critical influence of Young's modulus on erosion behavior.

Research question 4: How can the long-term lifetime of PA and PD be predicted, and what are their long-term lifetimes?

The long-term lifetime of PA and PD coatings can be predicted using Verma's long-term rain erosion

model. The predicted lifetime of the coatings is determined by the incubation period, meanwhile, the rain and wind statistics at a specific site are taken into account. A coastal location, Wilhelminadorp, was selected in this study. The DTU 10-MW wind turbine on which PA and PD coatings are applied was chosen.

In this research, the key focus the model is Springer's equation which is employed to determine the short-term damage rate (without considering rain and wind conditions). Hence, the material properties: density, speed of sound, ultimate tensile strength, and Poisson's ratio are required inputs to calculate the analytical surface fatigue. Additionally, the Wöhler slopes from the experimental $v - n_i$ and $v_{eq} - n$ curves are essential.

Through a weighted sum calculation of the short-term erosion damage rate for various rain and wind conditions, the long-term erosion damage rate and expected lifespan of the blade coating were determined. Similar to the experimental results, the lifetime of PD is longer than that of PA. Nonetheless, the prediction shows extremely short lifetimes for both coatings (less than 1.5 seconds) due to the breach of the lower limit and the upper limit of Springer's model.

However, adjusting the ultimate tensile strength of PD from 2.11 MPa to a more commonly observed value of 65 MPa for polymers significantly increased the predicted lifetime to 13.62 years for input m from $v - n_i$ (old method) and 1.05 years for input m from $v_{eq} - n_i$ (new method). This finding highlights the critical role of accurate ultimate tensile strength in the prediction process.

Additionally, the new method displays a lower lifetime than the old method, contradicting the experimental observations. This discrepancy can be attributed to the unsuitability of Springer's model for v_{eq}, as it neglects the magnification in velocity. Therefore, future improvements to the model are necessary to effectively incorporate the new method.

Research question 5: How sensitive is the lifetime of PA and PD to variations in ultimate tensile strength and Poisson's ratio in the long-term rain erosion model?

The sensitivity analysis conducted in this study confirms the high sensitivity of lifetime predictions to variations in ultimate tensile strength and Poisson's ratio, thereby emphasizing the importance of accurate input material properties for reliable lifetime predictions. PA and PD show similar sensitivity with increasing values of ultimate tensile strength and Poisson's ratio leading to a corresponding increase in the predicted lifespan of the coatings. Following Springer's equation, the lifetime changes exponentially with a power of 5.7 as the ultimate tensile strength varies. In the sensitivity analysis of Poisson's ratio, the variation in lifetime is more significant. Increasing the ultimate tensile strength from 70% to 130% of its original value leads to an increase in the lifetime from 1.78 to 60.74 years. In contrast, varying Poisson's ratio within the same range results in an increase from 1.64 to 411.10 years.

6

Recommendations

This thesis has proposed equivalent velocity to deal with the overlooked volume interdependence in the analysis of experimental results from the PJET and has conducted research on the use of the PJET has provided insights into the erosion behavior of advanced polymer coatings. However, there are still areas that require further investigation and improvement. Therefore, some recommendations are proposed:

- Validation of the equivalent velocity concept: The impact caused by a water slug in the PJET at the impact velocity may not be exactly equivalent to a spherical droplet with the same diameter at the corresponding equivalent velocity due to the differences in actual water slug length and shape. These differences in shape and length can lead to variations in the impact mechanism. For example, according to the literature [58], the contact force varies with impact time, indicating that even with the same kinetic energy, the impact on the surface may not be the same for different sizes of water droplets. Therefore, it is necessary to validate the analytical approach of equivalent velocity using experimental and numerical models.

- Improvement of experimental method: Instead of interrupting the erosion experiments at regular intervals, a continuous observation method should be adopted to reduce the additional effect of relaxation time. This can be achieved by implementing advanced imaging techniques or real-time monitoring systems to capture the erosion process accurately. Additionally, it is suggested to incorporate temperature and humidity control systems in the chamber, as environmental conditions can also influence erosion behavior. These factors can serve as independent variables in future experiments. Furthermore, conducting experiments with a wider range of impact velocities and increasing the number of measurements will provide more precise surface fatigue curves and improve the reliability of the analysis.

- Further research on properties and quality of materials: The sensitivity analysis emphasizes the importance of accurate material property measurements for reliable lifetime predictions. It is recommended to refine the measurement techniques, particularly under high strain rate conditions, to ensure the accuracy of the material properties used in the erosion model. In addition, the quality of samples should be improved to reduce initial surface defects.

- Refinement of the model: The leading-edge erosion model utilized in this study assumes homogeneity of the samples, neglecting the potential influence of underlying layers such as fillers and substrates. Therefore, it is recommended to incorporate the effects of these layers in future modeling efforts. Additionally, while the current model considers only the blade tip speed and the terminal velocity of the rain droplet, it is advisable to also account for the impact of wind on the velocity. Lastly, to enhance the model's suitability for the equivalent velocity, it is recommended to refine the equation by replacing the empirically fitted constants of Springer's equation with constants obtained from fitting available PJET results using the equivalent velocity method. Thereby

the number of impacts until incubation at a specific velocity can be adjusted in the denominator term of the damage rate to improve the accuracy of lifetime predictions.

References

[1] W. F. Adler. “Rain impact retrospective and vision for the future”. In: *Wear* 233 (1999), pp. 25–38.

[2] National Aeronautics and Space Administration. *How big can a raindrop get?* URL: https://gpm.nasa.gov/resources/faq/how-big-can-raindrop-get.

[3] International Energy Agency. *Wind electricity*. 2022. URL: https://www.iea.org/reports/wind-electricity (visited on 12/19/2022).

[4] B. Amirzadeh et al. “A computational framework for the analysis of rain-induced erosion in wind turbine blades, part I: Stochastic rain texture model and drop impact simulations”. In: *Journal of Wind Engineering and Industrial Aerodynamics* 163 (2017), pp. 33–43.

[5] D. Atlas, R. C. Srivastava, and R. S. Sekhon. “Doppler radar characteristics of precipitation at vertical incidence”. English. In: *Reviews of Geophysics* 11.1 (1973). Cited By :634, pp. 1–35. URL: www.scopus.com.

[6] A. C. Best. “The size distribution of raindrops”. In: *Quarterly journal of the royal meteorological society* 76.327 (1950), pp. 16–36.

[7] D. Chandler. *How to tame hammering droplets*. 2011. URL: https://energy.mit.edu/news/how-to-tame-hammering-droplets/.

[8] S. S. Cook. “Erosion by water-hammer”. In: *Proceedings of the Royal Society of London. Series A, Containing Papers of a Mathematical and Physical Character* 119.783 (1928), pp. 481–488.

[9] E. Cortés et al. “On the material characterisation of wind turbine blade coatings: the effect of interphase coating–laminate adhesion on rain erosion performance”. In: *Materials* 10.10 (2017), p. 1146.

[10] D. Čuha and M. Hatala. “Effect of a modified impact angle of an ultrasonically generated pulsating water jet on aluminum alloy erosion using upward and downward stair trajectory”. In: *Wear* 500 (2022), p. 204369.

[11] A. Dashtkar et al. “Graphene/sol–gel modified polyurethane coating for wind turbine blade leading edge protection: Properties and performance”. In: *Polymers and Polymer Composites* 30 (2022), p. 09673911221074197.

[12] A. Dashtkar et al. “Rain erosion-resistant coatings for wind turbine blades: A review”. In: *Polymers and Polymer Composites* 27.8 (2019), pp. 443–475.

[13] J. P. Dear and J. E. Field. “High-speed photography of surface geometry effects in liquid/solid impact”. In: *Journal of Applied Physics* 63.4 (1988), pp. 1015–1021.

[14] M. Alonso Diaz. *Leading Edge Erosion. Effect of droplet impact frequencies and dry intervals on incubation times of polyurethane coatings*. 2021. URL: http://resolver.tudelft.nl/uuid:e085cfb7-1fe1-47e9-b0f4-5d3bf4487d6a.

[15] DNVGL-RP-0171. “Testing of Rotor Blade Erosion Protection Systems”. In: (2018).

[16] L. Domenech et al. “Top Coating Anti-Erosion Performance Analysis in Wind Turbine Blades Depending on Relative Acoustic Impedance. Part 2: Material Characterization and Rain Erosion Testing Evaluation”. In: *Coatings* 10.8 (2020), p. 709.

[17] P. Dvorak. *Think polymer solutions when faced with erosion, corrosion, and abrasion*. 2017. URL: https://www.windpowerengineering.com/think-polymer-solutions-faced-erosion-corrosion-abrasion/.

[18] O. Edenhofer et al. “IPCC special report on renewable energy sources and climate change mitigation”. In: *Prepared By Working Group III of the Intergovernmental Panel on Climate Change, Cambridge University Press, Cambridge, UK* (2011).

[19] Armour Edge. *Leading Edge Erosion: A serious and expensive issue*. URL: https://armouredge.com/leading-edge-erosion/.

[20] M. Froese. *3M to launch Wind Protection Tape 2.0 at WindEnergy Hamburg*. 2016. URL: https://www.windpowerengineering.com/3m-launch-wind-protection-tape-2-0-windenergy-hamburg/.

[21] A. A. Fyall and R. B. King. *Proceedings of the rain erosion conference held at Meersburg, West Germany 5th - 7th May, 1965*. Royal Aircraft Establishment.

[22] D. T. Griffith and T. D. Ashwill. "The Sandia 100-meter all-glass baseline wind turbine blade: SNL100-00". In: *Informe Técnico, Sandia National Laboratories* (2011).

[23] K. K. Haller et al. "Computational study of high-speed liquid droplet impact". In: *Journal of applied physics* 92.5 (2002), pp. 2821–2828.

[24] W. Han, J. Kim, and B. Kim. "Effects of contamination and erosion at the leading edge of blade tip airfoils on the annual energy production of wind turbines". In: *Renewable energy* 115 (2018), pp. 817–823.

[25] L. Hartman. *Wind Turbines: the Bigger, the Better*. 2022. URL: https://www.energy.gov/eere/articles/wind-turbines-bigger-better (visited on 12/19/2022).

[26] S. Hattori and M. Kakuichi. "Effect of impact angle on liquid droplet impingement erosion". In: *Wear* 298 (2013), pp. 1–7.

[27] F. Heineke et al. *Renewable-energy development in a net-zero world*. 2022. URL: https://www.mckinsey.com/industries/electric-power-and-natural-gas/our-insights/renewable-energy-development-in-a-net-zero-world (visited on 12/19/2022).

[28] University CEU Cardenal Herrera. *Materials developed for the Project ROTOR BLADE EROSION EVALUATION TOOL (BEETOOL)*. Reference INNVA1/2021/57, funded by the Valencian Agency for Innovation (AVI), Generalitat Valenciana, Spain.

[29] R. Herring et al. *The increasing importance of leading edge erosion and a review of existing protection solutions*. 2019. URL: https://doi.org/10.1016/j.rser.2019.109382 (visited on 12/19/2022).

[30] N. Hoksbergen, R. Akkerman, and I. Baran. "The Springer Model for Lifetime Prediction of Wind Turbine Blade Leading Edge Protection Systems: A Review and Sensitivity Study". In: *Materials* 15.3 (2022). ISSN: 1996-1944. URL: https://www.mdpi.com/1996-1944/15/3/1170.

[31] M. Elhadi Ibrahim and M. Medraj. "Water droplet erosion of wind turbine blades: Mechanics, testing, modeling and future perspectives". In: *Materials* 13.1 (2019), p. 157.

[32] Koninklijk Nederlands Meteorologisch Instituut. *Achtergrondinformatie Maandoverzicht van het weer (MOW)*. 2021. URL: https://www.knmi.nl/kennis-en-datacentrum/achtergrond/achtergrondinformatie-maandoverzicht-van-het-weer-mow.

[33] IRENA. *Renewable capacity highlights*. 2021. URL: https://www.irena.org/-/media/Files/IRENA/Agency/Publication/2021/Apr/IRENA_-RE_Capacity_Highlights_2021.pdf?la=en&hash=1E133689564BC40C2392E85026F71A0D7A9C0B91 (visited on 12/19/2022).

[34] M. B. Lesser J. E. Field and J. P. Dear. "Studies of two-dimensional liquid-wedge impact and their relevance to liquid-drop impact problems". In: *Proceedings of the Royal Society of London. A. Mathematical and Physical Sciences* 401.1821 (1985), pp. 225–249.

[35] K. J. Jackson et al. "Innovative design approaches for large wind turbine blades". In: *Wind Energy: An International Journal for Progress and Applications in Wind Power Conversion Technology* 8.2 (2005), pp. 141–171.

[36] K. M. Jespersen et al. "High rate response of elastomeric coatings for wind turbine blade erosion protection evaluated through impact tests and numerical models". In: *International Journal of Impact Engineering* (2023), p. 104643.

[37] B. John et al. "Polyamide 6 fibers with superior mechanical properties: TPU coating techniques". In: *Sen'i Gakkaishi* 65.9 (2009), pp. 236–240.

[38] R. Jonsson. *Characterisation and validation of a pulsating jet erosion test*. 2007.

[39] L. Mishnaevsky Jr. “Toolbox for optimizing anti-erosion protective coatings of wind turbine blades: overview of mechanisms and technical solutions”. In: *Wind Energy* 22.11 (2019), pp. 1636–1653.

[40] L. Mishnaevsky Jr. et al. “Leading edge erosion of wind turbine blades: Understanding, prevention and protection”. In: *Renewable Energy* 169 (2021), pp. 953–969.

[41] M. H. Keegan, D. H. Nash, and M. M. Stack. *On erosion issues associated with the leading edge of wind turbine blades*. 2022. URL: http://dx.doi.org/10.1088/0022-3727/46/38/383001 (visited on 12/19/2022).

[42] A. Nag et al. “Influence of the frequency and flow rate of a pulsating water jet on the wear damage of tantalum”. In: *Wear* 477 (2021), p. 203893.

[43] A. Hojjati Najafabadi et al. “A new approach of improving rain erosion resistance of nanocomposite sol-gel coatings by optimization process factors”. In: *Metallurgical and Materials Transactions A* 45 (2014), pp. 2522–2531.

[44] D. Nash et al. “A staged approach to erosion analysis of wind turbine blade coatings”. In: *Coatings* 11.6 (2021), p. 681.

[45] Yes Painter. *What are putty and primer for?* 2020. URL: https://yespainter.com/faq-items/what-are-putty-and-primer-for/.

[46] F. Panetta. *Greener and cheaper: could the transition away from fossil fuels generate a divine coincidence?* 2022. URL: https://www.ecb.europa.eu/press/key/date/2022/html/ecb.sp221116~c1d5160785.en.html (visited on 12/19/2022).

[47] AC Plastics. *The Tensile Strength of Polycarbonate Sheeting*. URL: https://www.acplasticsinc.com/informationcenter/r/tensile-strength-of-polycarbonate.

[48] Professional Plastics. *Mechanical Properties of Plastic Materials*. URL: https://www.professionalplastics.com/professionalplastics/MechanicalPropertiesofPlastics.pdf.

[49] LM Wind Power. “On the leading edge: innovative solutions to reduce rain erosion”. In: *lmwindpower. com/storiesand-press/stories/innovation/on-the-leading-edge,(accessed: 13-February-2020)* (2015).

[50] Full Circle Wind Services. *Wind turbine blade repair – when, why and how.* 2022. URL: https://www.fullcirclewindservices.com/wind-turbine-blade-repair-when-why-and-how/.

[51] A. H. Sierra and E. G. Pérez. “Wind farm owner’s view on rotor blades—from O&M to design requirements”. In: *International Conference on Wind Turbine Rotor*. 2013.

[52] H. Slot. “A fatigue-based model for the droplet impingement erosion incubation period”. In: (2021).

[53] G. S. Springer. *Erosion by liquid impact*. Scripta Publishing Co., 1976.

[54] E. F. Tobin et al. “Comparison of liquid impingement results from whirling arm and water-jet rain erosion test facilities”. In: *Wear* 271.9-10 (2011), pp. 2625–2631.

[55] A. S. Verma et al. “A probabilistic long-term framework for site-specific erosion analysis of wind turbine blades: A case study of 31 Dutch sites”. In: *Wind Energy* 24.11 (2021), pp. 1315–1336.

[56] A. S. Verma et al. “A probabilistic rainfall model to estimate the leading-edge lifetime of wind turbine blade coating system”. In: *Renewable Energy* 178 (2021), pp. 1435–1455.

[57] A. S. Verma et al. “Leading edge erosion of wind turbine blades: Effects of blade surface curvature on rain droplet impingement kinematics”. In: *Journal of Physics: Conference Series*. Vol. 1618. 5. IOP Publishing. 2020, p. 052003.

[58] A. S. Verma et al. “Numerical investigation of rain droplet impact on offshore wind turbine blades under different rainfall conditions: A parametric study”. In: *Composite Structures* 241 (2020), p. 112096.

[59] E. H. Wong and Y. W. Mai. *Robust design of microelectronics assemblies against mechanical shock, temperature and moisture*. Woodhead Publishing, 2015.

[60] T. Yamagata, M. Hasegawa, and N. Fujisawa. “Erosion behavior of pulsed-jet test facility for wind turbine blade”. In: *Wear* 514 (2023), p. 204565.

[61] S. Zhang. “Accelerated rain erosion of wind turbine blade coatings”. PhD thesis. 2014. ISBN: 978-87-93054-49-3.

[62] S. Zhang et al. “Erosion of wind turbine blade coatings–design and analysis of jet-based laboratory equipment for performance evaluation”. In: *Progress in Organic Coatings* 78 (2015), pp. 103–115.

A

Comparison of measurements

Table A.1: Impact velocity vs. incubation period and breakthrough for PA and PD.

Velocity (m/s)	Incubation time (min)						Breakthrough (min)					
	PA			PD			PA			PD		
	Min.	**Avg.**	Max.	Min.	**Avg.**	Max.	Min.	**Avg.**	Max.	Min.	**Avg.**	Max.
140	45.0	**45.0**	45.0	76.4	**83.8**	96.9	-	**-**	-	-	**-**	-
145	-	**-**	-	-	**-**	-	60.0	**167.7**	369.7	-	**-**	-
150	30.0	**37.5**	60.0	15.0	**21.5**	30.2	61.9	**142.3**	185.4	60.0	**320.6**	618.5
160	15.0	**15.1**	15.4	14.2	**15.7**	16.7	44.1	**51.0**	60.0	60.4	**159.9**	300.4
170	-	**-**	-	-	**-**	-	-	**-**	-	61.7	**155.0**	316.2

B

Fitted equations of n_i vs. $\frac{S}{P}$

Table B.1: Comparison of experimental data's fitted curves with Springer's equation.

Springer's equation	$n_i = 7 \times 10^{-6}(\frac{S}{P})^{5.7}$
PA ($v - n_i$)	$n_i = 2.9037 \times 10^{3}(\frac{S}{P})^{8.1087}$
PA ($v_{eq} - v_i$)	$n_i = 3 \times 10^{9}(\frac{S}{P})^{5.4058}$
PD ($v - n_i$)	$n_i = 1.2414 \times 10(\frac{S}{P})^{12.613}$
PD ($v_{eq} - n_i$)	$n_i = 6 \times 10^{10}(\frac{S}{P})^{8.4085}$
PD ($v - n_i$, $\sigma_U = 65$ MPa)	$n_i = 2 \times 10^{-18}(\frac{S}{P})^{12.613}$
PD ($v_{eq} - n_i$, $\sigma_U = 65$ MPa)	$n_i = 1.88 \times 10^{-2}(\frac{S}{P})^{8.4085}$